Review

Yifan Qi and Yang Li*

Integrated lithium niobate photonics

https://doi.org/10.1515/nanoph-2020-0013
Received January 10, 2020; revised March 1, 2020; accepted March 4, 2020

Abstract: Lithium niobate ($LiNbO_3$) on insulator (LNOI) is a promising material platform for integrated photonics due to single crystal $LiNbO_3$ film's wide transparent window, high refractive index, and high second-order nonlinearity. Based on LNOI, the fast-developing ridge-waveguide fabrication techniques enabled various structures, devices, systems, and applications. We review the basic structures including waveguides, cavities, periodically poled $LiNbO_3$, and couplers, along with their fabrication methods and optical properties. Treating those basic structures as building blocks, we review several integrated devices including electro-optic modulators, nonlinear optical devices, and optical frequency combs with each device's operating mechanism, design principle and methodology, and performance metrics. Starting from these integrated devices, we review how integrated LNOI devices boost the performance of $LiNbO_3$'s traditional applications in optical communications and data center, integrated microwave photonics, and quantum optics. Beyond those traditional applications, we also review integrated LNOI devices' novel applications in metrology including ranging system and frequency comb spectroscopy. Finally, we envision integrated LNOI photonics' potential in revolutionizing nonlinear and quantum optics, optical computing and signal processing, and devices in ultraviolet, visible, and mid-infrared regimes. Beyond this outlook, we discuss the challenges in integrated LNOI photonics and the potential solutions.

Keywords: lithium niobate; integrated photonics; waveguide; resonator; electro-optic; nonlinear optics.

***Corresponding author: Yang Li,** Tsinghua University, Percision Instrument, Beijing, Beijing, China, e-mail: yli9003@mail.tsinghua.edu.cn.
https://orcid.org/0000-0002-1231-0538
Yifan Qi: Tsinghua University, Percision Instrument, Beijing, Beijing, China

1 Introduction

Lithium niobate ($LiNbO_3$, LN) is one of the most popular materials for electro-optic devices and nonlinear optical devices in the fast-growing field of integrated photonics [1]. Compared with traditional material platforms such as silicon [2, 3], silicon nitride [4, 5], and indium phosphide [6], LN has several natural advantages, including strong electro-optic effect (largest $r_{33} = 27$ pm/V at 1500 nm), large refractive index ($n_o = 2.21$ and $n_e = 2.14$ at 1550 nm), wide transparency wavelength (from 400 nm to 5 μm), and stable physical and chemical characteristics [7], thus making it the most competitive material for linear and nonlinear integrated photonics.

Exploring LN in integrated photonics begun in the last century. In 1974, Schmidt and Kaminow [8] attempted to make integrated waveguides in LN by using metal-diffusing processes, which later became the most common method in nanostructuring LN. As the development of metal-diffusing processes, titanium diffusion stood out and became the most commonly used one due to the fact that titanium diffusion can provide a relatively high refractive index contrast (~0.04) and a small effective diffusion depth (~1.6 μm) [8–11]. Another traditional method for nanostructuring LN is proton exchange, which can achieve similar structure and performance as those provided by titanium diffusion [12–14].

Titanium diffusion and proton exchange opened the door of exploring the outstanding performance of LN in integrated photonics. However, we still cannot fully leverage LN's extraordinary optical properties because those processing techniques place a lower limit on the waveguide's diameter of approximately 10 μm, and an upper limit on refractive index contrast of 0.1 [1, 14–16]. Based on a waveguide with width over 10 μm, it would be challenging to realize the design of single-mode waveguide and integrated photonic circuits in the visible and near-infrared (IR) regimes. Moreover, the low refractive index contrast induces a weak field confinement [17–19], degrading the performance of many devices, such as increasing bending losses of waveguides, increasing length of Mach–Zehnder interferometer (MZI) arms of modulators, as well as decreasing Q factors and increasing mode volumes of resonators.

Similar to silicon on insulator (SOI), LN on insulator (LNOI) consists of a submicrometer LN film on a silica buried layer, which is on top of a substrate made from silicon or LN. Fabrication of LNOI has been achieving a fast development in the past two decades [20, 21]. To fabricate an LNOI, a single-crystal submicrometer LN film is first obtained by ion slicing a bulk crystal and then is bonded to a low index substrate by using benzocyclobutene bonding [22] or crystal bonding [23]. Such a fabrication process has already become mature, leading to the commercialization of LNOI wafers. A typical LNOI wafer has an LN film thickness of hundreds of nanometers (typically 300–900 nm) and a diameter of 3 or 4 inches [24]. Along with the development of LNOI, nanostructuring of LNOI has been developing rapidly since 2007 [25]. Nowadays, several techniques including wet etching, dry etching, chemical mechanical polishing (CMP), diamond dicing, femtosecond laser direct writing, and focused ion beam (FIB) milling have been applied to the nanostructuring of LNOI [26–38]. All these techniques enable fabricating LN ridge waveguides or structures (will be called "ridge structures" for short in the rest of this review) on LNOI platform. Ridge structures have the following advantages over structures made by using titanium diffusion and proton exchange [39]:

(1) High refractive index contrast. Conventional LN components made from bulky LN materials by titanium diffusion or proton exchange have an index contrast as small as ~0.1. In contrast, because ridge structures are made by directly structuring LN film, index contrast is determined by the difference between the refractive index of LN and that of the background medium. For LNOI with silica superstrate and substrate, the index contrast is ~0.7 and can be further increased to over ~1 if the silica superstrate is removed. Such a high index contrast brings several advantages including strong field confinement and low bending loss.

(2) Flexibility in fabricating nanostructures. Compared with titanium diffusion and proton exchange, ridge structure brings a high degree of flexibility to the fabrication of LN nanostructures. Such flexibility not only enables fabricating waveguide on the submicrometer scale, but also allows fabricating various structures, such as microring, periodically poled LN (PPLN) [40], and photonic crystal [41].

By fully leveraging the high index contrast and flexibility provided by ridge structures, we can integrate various structures, devices, and systems onto a single LNOI chip, reaching a high degree of multifunctionality, flexibility, and scalability (Figure 1). This review focuses on the new physics, new methods, and new applications that LNOI and ridge structures bring to the field of integrated LN photonics.

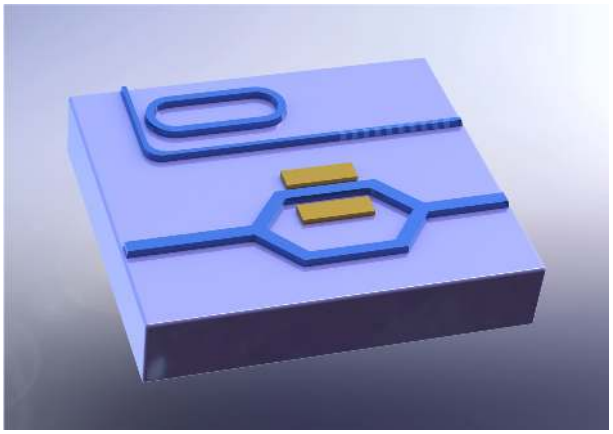

Figure 1: Schematic view of an integrated LNOI photonics chip. Waveguides, resonators, periodically poled lithium niobate, modulators, and many other structures and devices can be integrated onto a single LNOI chip to achieve various systems and applications.

This review is structured as follows: Section 2, Basic structures, introduces the basic structures including waveguides, resonant cavities, structures for nonlinear optics, and optical coupling, as well as their design methods, fabrication processes, and several classical examples. Based on these structures as building blocks, Section 3, Integrated devices, introduces several integrated devices, including electro-optic modulators, nonlinear optical devices, and optical frequency combs, and analyzes their principles and performance. Section 4, Systems and applications, reviews the current status and envisions the prospects of several integrated LN systems, including optical communication systems, integrated microwave photonics systems, quantum optics systems, metrology systems, and their applications. Section 5, Summary and outlook, summarizes this review and envisions LNOI devices' potential applications in high-performance nonlinear and quantum optics, optical computing, and signal processing, as well as devices in ultraviolet (UV), visible, and mid-IR regimes. This section then discusses the challenges in integrated LN photonics and the potential solutions.

2 Basic structures

Various integrated optical devices can be fabricated based on LNOI and ridge structures. These devices have certain similarities in basic structure and fabrication process despite their different designs, mechanisms, and

functionalities. In this chapter, we introduce the basic building blocks for integrated optical devices, including optical waveguide, resonant cavity, PPLN, and coupling structures. Those structures do not cover all the LN nanostructures but are the most basic components for building a wide variety of integrated LN optical devices.

2.1 Optical waveguide

Waveguide is one of the most fundamental components that consist of integrated optical devices. Waveguide can compose an MZI as the main structure of electro-optic modulators or construct a microring for a resonant cavity or build devices that propagate and process light on a photonic chip. Traditional LN waveguides are typically fabricated by using titanium diffusion and proton exchange. The structure of traditional LN waveguide is shown in Figure 2A, giving an indistinct boundary and a small index contrast between waveguide region and regular LN region. To overcome the limitations of the traditional waveguide structure, LN ridge waveguide was proposed, as shown in Figure 2B. Ridge waveguide brings the following advantages: (1) distinct physical boundary between waveguide and background medium, such as air and silica; (2) the waveguide geometry including width and aspect ratio can be defined with a high degree of flexibility; (3) the index contrast can be tuned by depositing a superstrate above the waveguide [39, 42, 43].

2.1.1 Manufacturing method

In the early days, wet etching was used for the direct etching of LN ridge waveguides. A chromium film is deposited on top of an LN film as a mask for the waveguide and is patterned by lithography. Then, the LN is wet etched by corrosive liquid, for example, a solution of 40% HF and 100% HNO_3. In a classic work, by using wet etching, an LN waveguide was fabricated with a top width of 6.5 μm, showing a propagation loss of 0.3 dB/cm at 1550 nm [44]. Wet etching is used not only for etching LN thin films, but also for nanostructuring titanium-diffused or proton-exchanged LN thin films. Wet etching is also used to improve the sidewall roughness of a waveguide caused by the residual of photoresist mask. For example, a 60-min wet etching with NH_4OH, H_2O_2 and H_2O mixed by 2:2:1 at 85°C was proved to be efficient to remove material deposition [45]. A similar process was applied in Escale et al. [46]. However, most wet etching processes are chemical and isotropic, which may lead to a tilted sidewall. Furthermore, the isotropic property of wet etching makes it hard to fabricate waveguides narrower than 1 μm. And, considering wet etching's extremely low etching rate of X-cut LN thin film (3 nm/h) [44], wet etching is being used less and less nowadays, especially after the rapid development of dry etching and X-cut LN.

Dry etching is the most popular and promising method for fabricating a high-quality waveguide in thin film LN. Dry etching LN has been of great interest to the integrated photonics community for many years. In the early days of LN nanofabrication, dry etching LN bulky crystal did not attract much attention because of the chemical stability of LN [47, 48]. However, along with the availability of LNOI wafers and the rapid development of dry etching technique, the state-of-the-art dry etching technique has already been able to realize submicron scale waveguide with low loss on LNOI [49].

The dry etching process is shown in Figure 3. Fabricating a waveguide starts with a commercially available LNOI wafer. First, an etching mask is deposited on the top of the LNOI. In this step, chromium [48], amorphous silicon [50], or other kinds of resist [49, 51] have been used according to different processes. Second, photonic patterns are defined in the etching mask using different methods including electron-beam lithography (EBL) or

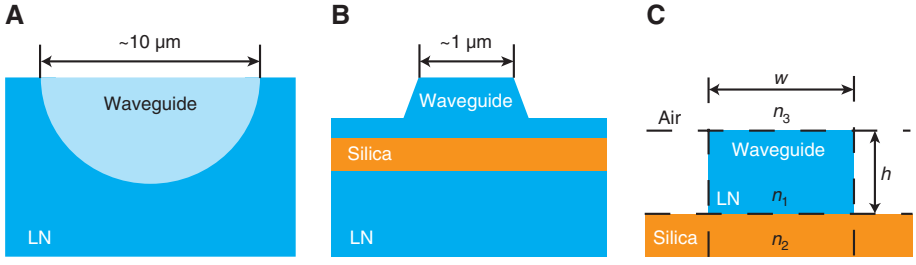

Figure 2: Schematic cross-section view of integrated LN waveguide.
(A) Conventional LN waveguide; (B) LNOI ridge waveguide; (C) ideal LNOI waveguide.

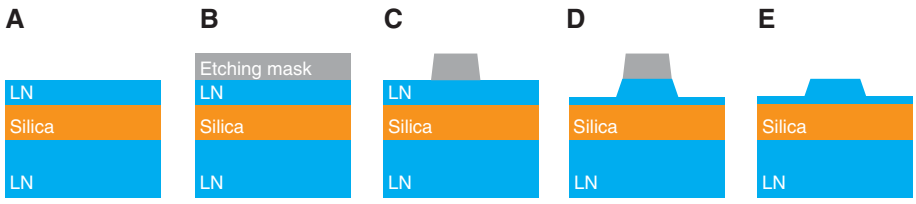

Figure 3: A standard dry etching process of LNOI.
An LNOI wafer (A) is first deposited with an etching mask (B). Then, the etching mask is patterned by using electron-beam lithography (C) to define the geometry of structure. Using reactive ion etching (RIE) or inductively coupled plasma RIE (ICP-RIE), the lithium niobate outside the waveguide area is etched away (D). Finally, etching mask is removed (E) and the waveguide is formed.

photolithography. In order to improve the selectivity of etching or to improve the sidewall roughness [52], annealing is performed in some cases [53].

The third and the most important step is etching LNOI thin film for obtaining the waveguide structure. Reactive ion etching (RIE) and/or inductively coupled plasma RIE (ICP-RIE) is commonly used for dry etching LNOI. Several different gases are used for chemical etching. Fluoride gas, which is commonly used in chemical reaction etching of many materials, is sometimes used in etching LN. And, because of the chemical stability of LN, using argon (Ar) plasma only for physical etching is also a common practice [21, 50, 53–55]. Selecting different gases can affect the etching process and results, such as surface roughness of the waveguide [52, 56]. Recently, Ar^+ became the most frequently used gas because by physical etching Ar^+ can induce a more vertical sidewall despite the fact that Ar^+ extends the etching time. When a certain gas is selected, other etching parameters, such as ICP power, RIE power, gas flow rate, pressure, and temperature, also have a great influence on the processing speed, etching depth, surface roughness, and sidewall angle [45]. According to the current processes, it is still difficult to realize a completely vertical waveguide sidewall by using dry etching, but such a vertical sidewall is not always necessary from the application point of view. After dry etching, etching mask is removed and the fabrication process is complete.

In addition to wet etching and dry etching, many other methods have also been used for processing waveguides in LNOI. Chemical mechanical polishing is a method believed to provide a surface as smooth as that fabricated by dry etching. Chromium layer is used as a mask in CMP method and is patterned by femtosecond laser ablation to define the shape of the waveguide. Then, by using a wafer polishing machine, the exposed LN film can be removed to form the waveguide. Finally, the chromium layer on top of the LN waveguide can be removed by using wet etching with HF solution [57]. Such a process is shown in Figure 4. By controlling the duration of CMP process, the sidewall angle can be adjusted from a few degrees to nearly 80° [58]. If the upper surface of the waveguide needs to be very smooth, a second CMP process can be performed. Chemical mechanical polishing process has achieved a waveguide with a root-mean-square surface roughness as low as 0.452 nm and a low loss of 0.1 dB/cm [59].

A direct machining method – diamond dicing – can also be used to fabricate ridge waveguides on LNOI (Figure 5). The sidewall angle of waveguides made by diamond dicing is defined by the shape of the diamond cutting blade. A waveguide with a high aspect ratio can be made by diamond dicing, but the width of the waveguide and the minimum distance between two neighboring waveguides are largely limited by the shape of the cutting blade [60].

Femtosecond laser direct writing and FIB milling have also been used in nanostructuring LNOI [61, 62]. By using those fabrication techniques, LN thin film and silica substrate can be ablated at the same time.

The key point of above methods is etching or removing LN outside the waveguide region to form the ridge waveguide, which is usually being processed under very careful control. To avoid this process, the effect of ridge waveguide can also be realized by a structure called “rib loaded waveguide” (Figure 6). Such a waveguide can be fabricated by using additive manufacturing. This fabrication process begins with coating LNOI with a film of the loaded material and is followed by etching the loaded material to form the rib. Because the loaded material can be selected from materials that are easy to etch, etching the loaded materials is always easier than etching LN directly. The most common choices for the loaded material are silicon nitride [35, 40, 63, 64] and chalcogenide glasses [33], whereas tantalum pentoxide (Ta_2O_5) [27] and titanium dioxide (TiO_2) [65] are also popular choices. To increase the ratio of light propagating in the LN film, the loaded rib can be designed as thin as tens of nanometers [65]. However, rib loaded waveguide usually suffers from a larger mode volume and a high propagation loss.

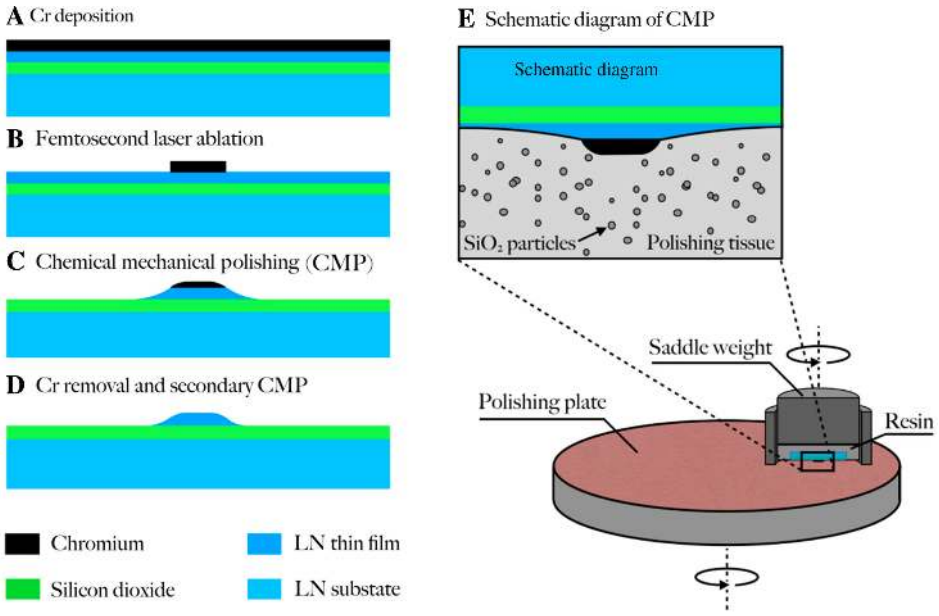

Figure 4: A standard fabrication process of chemical mechanical polishing (CMP).
(A) Cr thin film is first deposited on a LNOI wafer and is ablated by femtosecond laser (B) to define the pattern. Then, CMP is implemented (C) to polish lithium niobate thin film. Finally, Cr mask is removed by wet etching and secondary CMP is implemented for a smoother surface (D). (E) shows a schematic diagram for the CMP process. Reprinted with permission from Wu et al. [57].

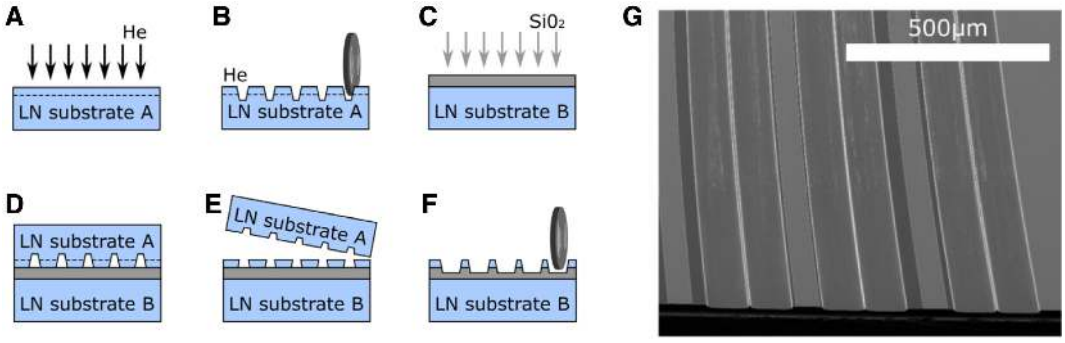

Figure 5: A standard fabrication process of diamond dicing.
(A–F) Show the standard fabrication process of diamond dicing and (G) shows a scanning electron microscope photograph of the waveguide made by using diamond dicing. Reprinted with permission from Volk et al. [60]. © The Optical Society.

2.1.2 Mode properties

The ridge waveguide shown in Figure 2B can be approximated as a rectangular waveguide in theoretical analysis. Such a rectangular waveguide with vertical sidewall (Figure 2C) can be modeled by the Marcatili method, giving the maximum number of modes [66]:

$$N_{\max} = 2 + \sqrt{\frac{2k^2wh(n_1^2 - n_2^2)(n_1^2 - n_3^2)}{\pi^2}} \quad (1)$$

where k is the wave number of the light guided in the waveguide; w, h, n_1, n_2, and n_3 are defined in Figure 2C. Unless the waveguide cross section is sufficiently small (width is less than ~400 nm for a 600-nm-thick LN film), the fundamental transverse electric (TE) and transverse magnetic (TM) modes are always supported at an operating wavelength of 1550 nm. As a result, a "double-mode" waveguide is a reasonable design in balancing the propagation loss and fabrication feasibility. "Double-mode" condition depends on many parameters including LN film thickness, etch depth, sidewall angle, and coating material. In general, waveguide width, which can meet the "double-mode" condition, decreases as the LN film thickness increases, etch depth decreases, tilt angle of sidewall increases, and refractive index of the coating material decreases. For example, a typical LNOI ridge waveguide with 600-nm LN film thickness, 350-nm etch depth, 70°

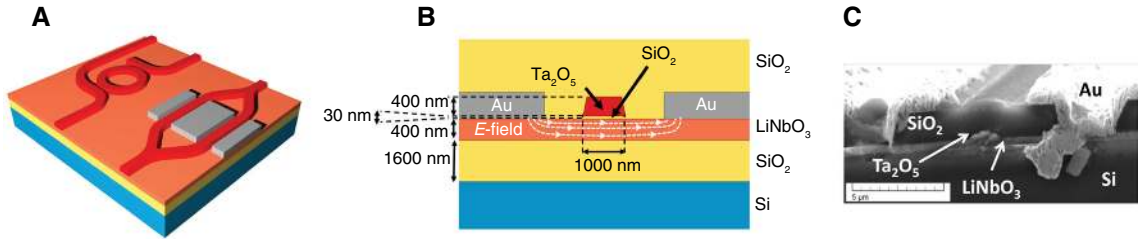

Figure 6: Rib loaded waveguides with Au electrodes.
(A) Schematic view, (B) cross section, and (C) scanning electron microscope image. Reprinted with permission from Rabiei et al. [27]. © The Optical Society.

sidewall angle, and silica coating does not support a second-order TE mode when the waveguide top width is less than 1 μm; that is, the "double-mode" condition is met. A low-aspect-ratio waveguide supports TE modes better, that is, the TE modes with a higher mode index and a lower propagation loss. Figure 7 shows the modes supported by a waveguide with top width 1 μm, height 600 nm, and sidewall angle ~80° at an operating wavelength of 1550 nm.

To make sure that only the fundamental TE or TM mode propagates in the "double-mode" waveguide, we need to carefully control the mode and polarization of the input light. From the viewpoint of the mode, we do not have to etch all the LN film outside the waveguide region (which is hard when certain masks are used). A larger etch depth reduces the propagation loss, but does not necessarily improve all the device merits, for example, for integrated LN electro-optic MZI modulators, microwave field in the waveguide decreases as the etch depth increases [67].

2.1.3 Propagation loss

Low-loss waveguide is the key to achieve high-performance integrated optoelectronic devices, such as electro-optic modulators with low drive voltage and broad bandwidth. Different from silicon-based optoelectronic devices [68], LN devices do not need doping to change the refractive index, so absorption losses caused by interband absorption and free carrier absorption are avoided, which is one of the unique advantages of LN. Because of the absorption of LN crystals, propagation loss of LN waveguide has a theoretical limitation down to ~0.001 dB/cm [57, 69]. So far, even the best LN waveguide shows a loss higher than this limitation. Two major sources of losses for integrated LN waveguides are radiation loss caused by waveguide bending and scattering loss induced by surface roughness. For a given waveguide, different modes have different losses. Generally speaking, due to fact that the confinement of higher-order modes is weaker than that of lower-order modes and that higher-order mode is closer

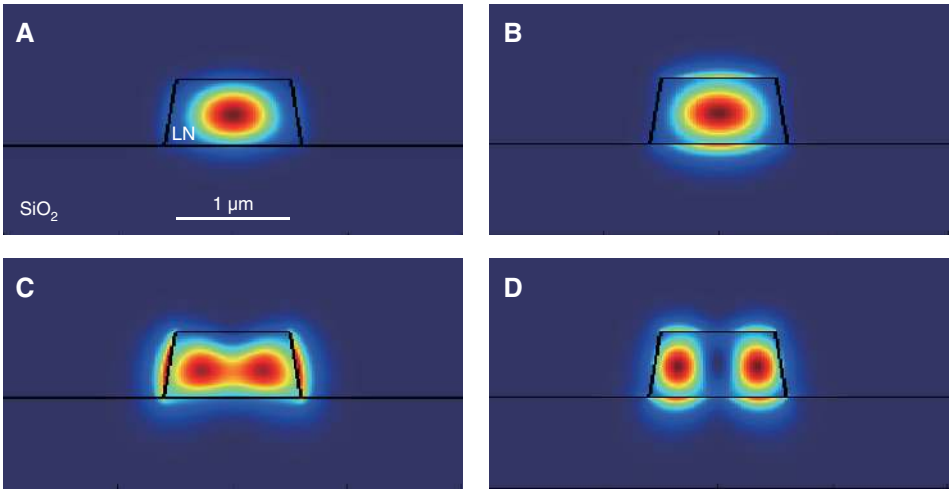

Figure 7: Calculated electric field intensity distribution of a direct etched LNOI waveguide with top width 1 μm, height 600 nm and sidewall angle ~80°.
The figures are field profile for (A) fundamental TE mode, (B) fundamental TM mode, (C) second-order TE mode and (D) second-order TM mode. The black lines indicate the profile of the waveguide and substrate.

to the cutoff condition, higher-order modes show higher radiation loss and scattering loss [66].

We can measure the loss of integrated LN waveguide by using several different methods. The most popular method is measuring the quality (Q) factor of a microring whose cross section is the same as the waveguide. As shown in Figure 8A, when a continuous wave (CW) light is critically coupled into the microring, waveguide loss can be calculated via $\alpha = 2\pi n_{\text{eff}}/(Q\lambda)$, where n_{eff} is the mode index, and λ is the resonant frequency [57]. This method is particularly suitable for low-loss waveguides, corresponding to high-Q microrings whose Q factor can be measured accurately. Cut-back method is an alternative and simple way for measuring waveguide loss. By measuring transmission power of waveguides with different lengths, we can obtain the propagation loss by calculating the slope of transmission versus waveguide-length curve, as shown in Figure 8B [66, 70]. Interferometric method is another way for measuring waveguide loss (Figure 8C). A waveguide with two polished end faces can be treated as a Fabry–Pérot resonator. So, the transmitted power changes periodically as a function of the round-trip phase, which can be tuned via thermo-optic or electro-optic effect. And, we can obtain the attenuation constant α of the waveguide by measuring the contrast K (also called visibility or modulation depth) of the Fabry–Perot interference [71, 72].

Along with the development of fabrication techniques for integrated LNOI waveguide, loss of LN waveguide has been improving significantly. A Si_3N_4 rib loaded waveguide shows a low loss of 0.32 dB/cm [63]. Furthermore, waveguides fabricated by direct etching [69] and by using CMP [57] both can show a record low loss of 0.027 dB/cm. Such a loss is negligible for integrated devices with footprints on the scale of tens to hundreds of μm^2.

2.2 Resonant cavity

Resonant cavity has board applications including optical sensing, optical communications, nonlinear optics [73, 74], and quantum optics [75]. The basic structures of LNOI cavity include microdisk (Figure 9A) and microring (Figure 9B). In recent years, as the maturity of fabrication technique of LNOI ridge structure, the quality of microring increases dramatically.

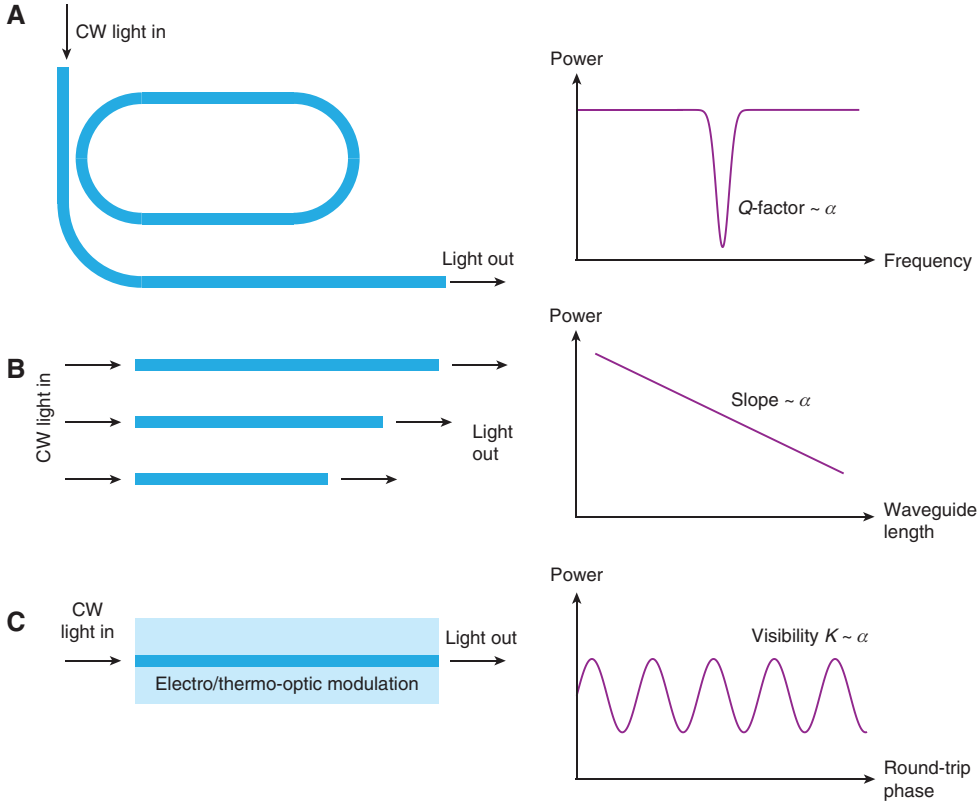

Figure 8: Schematic diagrams of measuring waveguide loss by different methods.
The figure above describes the principle and ideal measurement results for (A) microring method, (B) cut-back method, and (C) interferometric method, respectively.

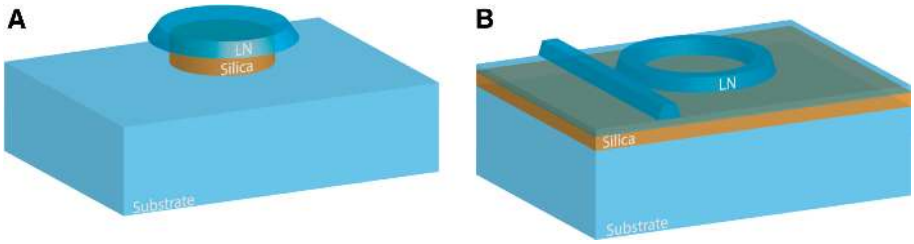

Figure 9: Schematic diagrams of LNOI resonant cavities.
(A) Microdisk resonator; (B) Microring resonator.

2.2.1 Microdisk resonators

Microdisk resonators are also known as whispering gallery mode (WGM) resonators because this type of resonators based on LNOI has the same physical principle as WGM resonators based on other platforms, such as optical fibers [76, 77]. As shown in Figure 10, the structure of the resonator is a solid microdisk made from LN thin film with a diameter of tens of micrometers. In order to improve the input and output coupling efficiency with fiber or waveguide and to better confine the WGM mode within the cavity, surface of the silica underneath the LN microdisk is removed by wet etching after processing the microdisk [78].

Several processing methods can be used to fabricate microdisk resonators, including dry etching [78], CMP [79], FIB milling [80], and femtosecond laser ablation [61, 62]. Based on those methods, the processing flows for fabricating LNOI microdisks are almost the same as those for manufacturing LNOI waveguides. The only difference is that microdisk does not necessitate fabricating vertical sidewalls. Some microdisks with highly angled sidewalls still can show good performance. For example, a microdisk with a wedge angle of 9.5 degrees shows a Q factor greater than 10^7 [58]. Furthermore, femtosecond laser ablation enables fabricating some complicated designs. For example, a double-layer microdisk resonator can be realized by ablating for only one time [62].

High-quality coupling of light into and out of the LNOI microdisk cavity is a key to improving performance. The coupling method used most frequently is based on tapered fiber, which is made by stretching a single-mode coating-removed optical fiber to a diameter of several microns by using flame annealing. By closely attaching the tapered region of the fiber to either sidewall or edge of the top (or bottom) surface of the microdisk, we can efficiently couple light from a laser, which is connected to one end of the fiber, to the microdisk [61, 78, 80, 81]. The other end of the fiber is usually connected to a photodetector. More details of tapered fiber coupling can be found in Cai et al. [82].

2.2.2 Microring resonators

Lithium niobate microring resonators guide light via a closed loop of LN waveguide. Compared with microdisk resonators, microring resonators have a significant advantage: a microring can be made by closing the loop of a waveguide. Such an advantage brings a great degree of flexibility to the design of microring – we can engineer microring's shape according to the particular requirement of the device (Figure 11) [83]. For example, to achieve an electro-optic frequency comb with long electrodes, we can design a racetrack-shaped microring [84].

Guided modes of a microring resonator are identical to those of curved waveguides, as discussed in Section 2.1.2, Mode properties. A typical LN microring is achieved in Guarino et al. [25], which is believed to be the first

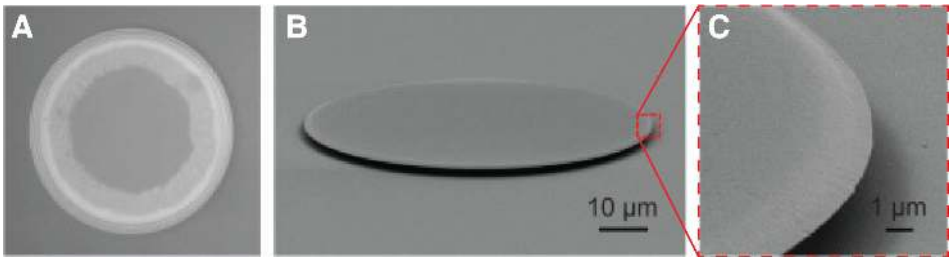

Figure 10: Microscope images of a typical LNOI microdisk resonator.
(A) Optical microscope image of the microdisk from the top. (B) scanning electron microscope image showing the overview and (C) the edge of the microdisk. Reprinted with permission from Wang et al. [51]. © The Optical Society.

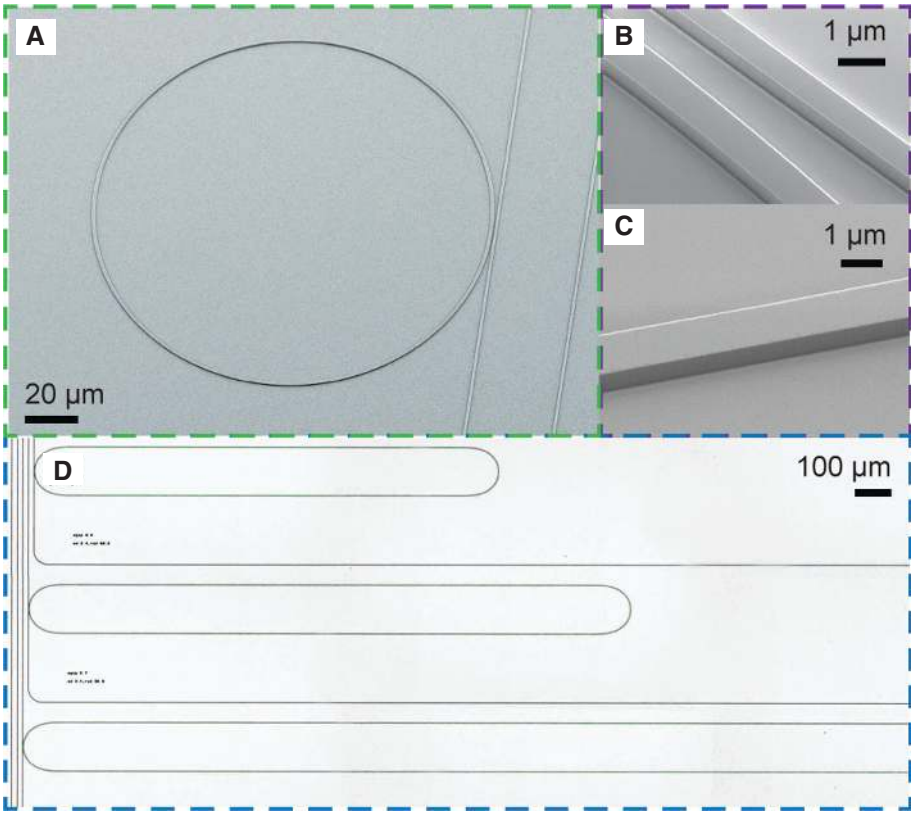

Figure 11: Several typical LNOI microring resonators.
(A) Scanning electron microscope of a typical LNOI microring. (B, C) Scanning electron microscope images of waveguides constituting microrings. (D) Optical microscope images of racetrack resonators with different lengths. Reprinted with permission from Zhang et al. [69]. © The Optical Society.

breakthrough in integrated LNOI photonics. We usually couple light into and out of a microring resonator by using waveguide coupling, which designs a waveguide along one side of the resonator, achieving coupling via the overlapping of the evanescent tail of the waveguide mode and that of the microring-resonator mode in the region where waveguide closes to the microring (Figures 9B and 11A, B) [85]. Because the position and shape of the waveguide can be designed carefully, microring resonator can achieve a high coupling efficiency, resulting in high device performance [25]. Moreover, by designing the waveguide cross section and by utilizing birefringence, dispersion of a microring can be engineered for nonlinear applications, which is discussed in Section 3.2, Nonlinear optics [86].

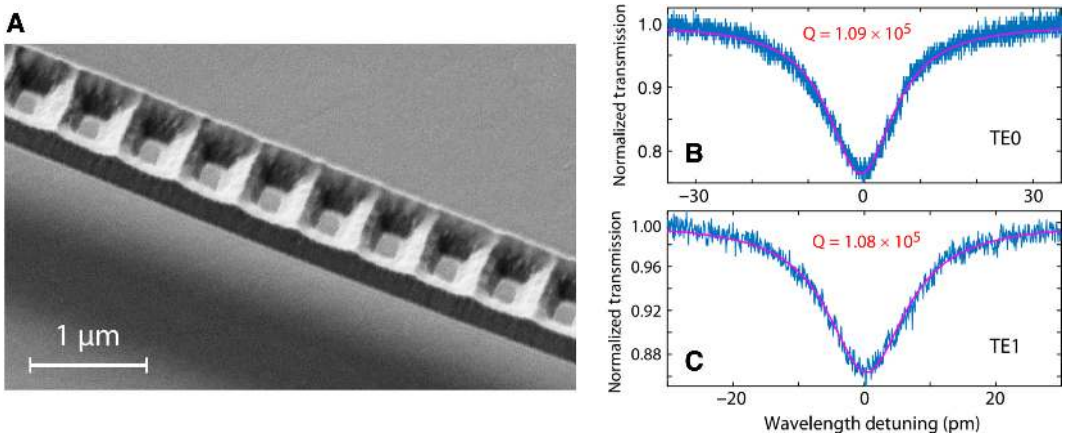

Figure 12: LNOI photonic crystal nanocavities.
(A) Scanning electron microscope image of an LN photonic crystal nanobeam. (B, C) Measured Q factors of the fundamental (TE0) and second-order (TE1) cavity modes. Reprinted with permission from Liang et al. [41]. © The Optical Society.

2.2.3 Photonic crystal nanocavities

Photonic crystal is dielectric periodic structure which can be designed to manipulate the behavior of light. For example, photonic crystal can be designed with photonic bandgaps to stopping light from propagating in certain directions in a particular range of frequency [87]. A one-dimensional photonic crystal nanobeam cavity can show a high Q factor and a high transmission to the feeding waveguide [88]. Such a cavity can be fabricated based on the LNOI ridge structure and dry etching process. As shown in Figure 12, a high-quality LN photonic crystal nanobeam cavity shows a Q factor of 10^5 [41] and has already been improved recently to 1.41×10^6 [89]. This nanobeam cavity demonstrates second-harmonic generation (SHG) and sum-frequency generation (SFG) with pump power around tens of microwatts [90]. In addition to SHG and SFG, photonic crystal nanocavities can also achieve several other applications such as extreme photorefractive effect [41].

2.2.4 Quality factor

Quality factor (Q), or Q factor, is an important metric for evaluating the quality and performance of a resonator. A higher Q factor means that the resonator can "lock" more energy for a given input–output coupling efficiency. Q factor is determined by the material and structure of the resonator, the fabrication precision, and coupling efficiency. In 2007, an LNOI microring resonator made by using photolithography shows a Q factor of 4×10^3 and the capability of electro-optic tunability [25]. For the time being, the photolithography technology limits the width of the waveguide as large as 4 μm, resulting in an multimode waveguide. In 2014, two LNOI microdisk resonators were demonstrated: one with a diameter of 28 μm shows a Q factor up to 1.02×10^5 [78], whereas the other with a diameter of 70 μm depicts a Q factor up to 4.84×10^5 [91]. In 2015, an LNOI microdisk with a Q factor of 1.19×10^6 was demonstrated [51], enabling the applications in electro-optic modulation and SHG. In 2017, a microring resonator with extracted propagation loss as low as 2.7 dB/m and Q factor up to 10^7 was realized [69], enabling applications in Kerr frequency comb and modulation [92]. Using CMP, a resonator with a Q factor of 1×10^7 was achieved [93], whereas another one with an even higher Q factor up to 4.7×10^7 was demonstrated [79]. Nowadays, Q factor of LN microring is higher than that of most other materials and is even comparable to microrings made from silica and silicon nitride.

Based on a double-layer microdisk resonator as in Figure 13, Zheng et al. [94] demonstrated an exterior whisper-gallery-mode resonator whose mode exists in the slot waveguide between two LN microdisks. Such a structure achieves a high Q factor of 10^5 and a large mode overlap with ambient environment, which is especially suitable for optical sensing. More discussion can be found in Section 5.2, Devices in UV, visible, and mid-IR regimes.

2.3 Periodically poled LN structures

Lithium niobate's high second-order nonlinear coefficient $\chi^{(2)}$, wide transparent window, and stable physical and chemical properties make LN the ideal material for second-order nonlinear optical interactions including SHG, SFG, and difference frequency generation (DFG) [95–98]. Phase matching (i.e. the need for interacting waves to have the same phase velocity) is necessary for generating nonlinear processes over a long interaction length. Quasi–phase matching compensates the phase velocity mismatch of the interacting waves by periodically adjusting the polarization direction [99]. Quasi–phase matching can be realized in LN by periodically reversing the $\chi^{(2)}$ sign [100], leading to a PPLN. Periodically poled LN can fully leverage the powerful nonlinear effects of LN. Combining the quasi–phase matching of PPLN with the strong field confinement of waveguide creates an efficient platform for nonlinear optical processes including SHG, SFG, and DFG. Those nonlinear optical processes enabled various applications including wavelength converters, optical parametric oscillators [101], digital signal processing [102], entangled photon pair generation [103], and supercontinuum generation [74, 104]. Periodically poled LN waveguides fabricated by titanium diffusion or proton exchange are limited by the weak field confinement and large mode volume, resulting in low nonlinear efficiency and long interaction length [105]. The development of LNOI ridge waveguide gives new life to PPLN. With a large index contrast, a smaller mode volume can be achieved in a nanostructured PPLN waveguide [106], increasing the SHG efficiency for over 20 times [107]. Applications of PPLN waveguides in nonlinear optics will be further discussed in Section 3.2.1, Nonlinear optics.

Periodically poled LN is made by using static electric field to invert the orientation of the ferroelectric domains in LN thin film (Figure 14). This method is suitable for Z-cut waveguides that support TM polarization (Figure 14A) and X-cut waveguides that support TE polarization (Figure 14B) with slightly different fabrication flows. The core of this method is to design positive and negative electrodes in the

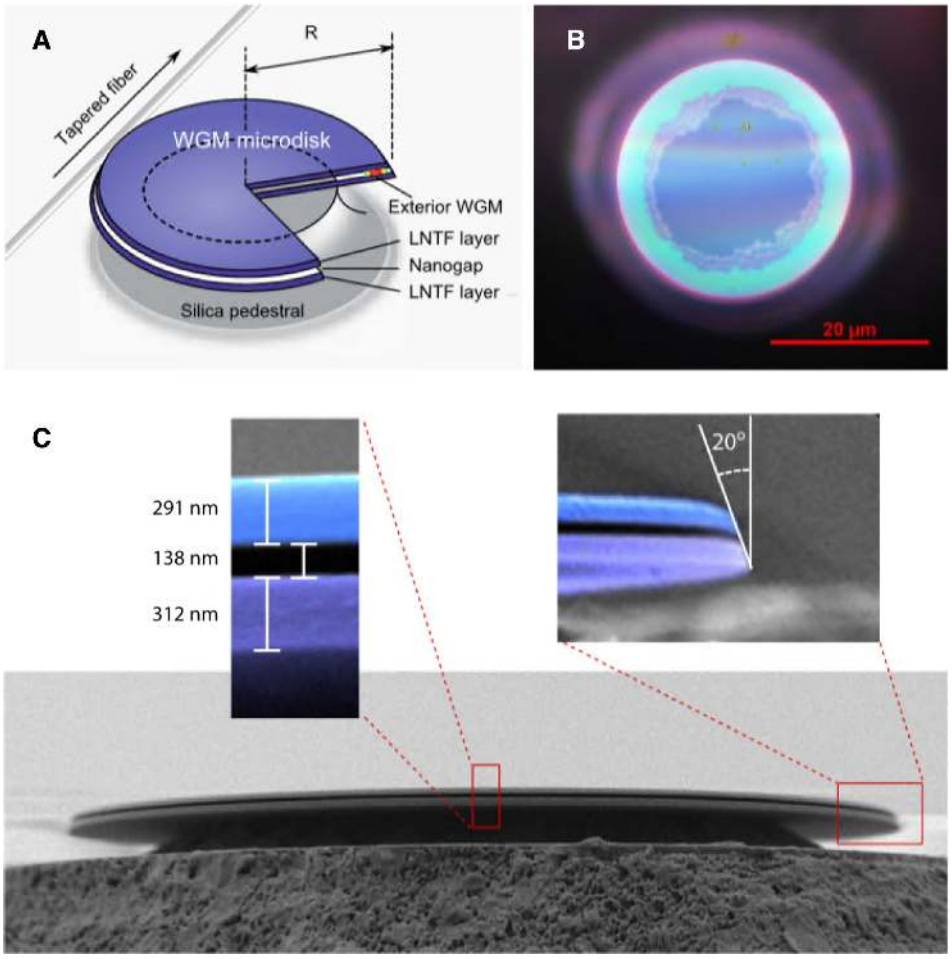

Figure 13: A double-layer LNOI microdisk resonator.
(A) Schematic of the double-layer LNOI microdisk resonator. (B) Top-view optical microscopy image of the microdisk. The two inner irregularly shaped circles indicate inward etching of the silica buffer layers. (C) Scanning electron microscope image of the microdisk, with enlarged false-colored images clearly showing the well-separated upper and lower LN thin film layers. Reprinted (abstract/excerpt/figure) with permission from Zheng et al. [94]. Copyright (2019) by the American Physical Society.

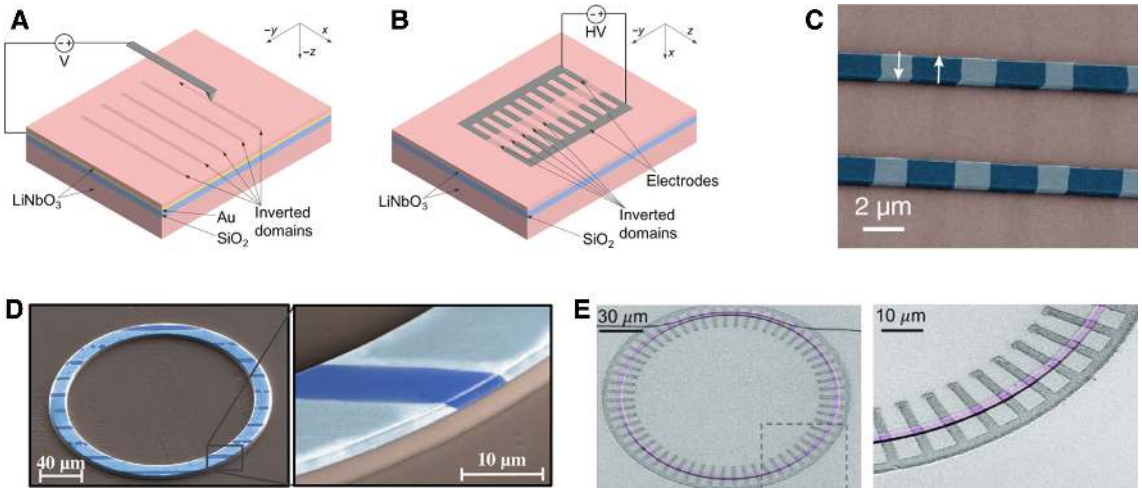

Figure 14: Fabrication procedures and results of PPLN structures.
(A, B) Schematic diagrams of fabricating PPLN on (A) Z-cut LN thin film and (B) X-cut LN thin film. Reprinted with permission from Boes et al. [42]. (C–E) False-color scanning electron microscope images of (C) the X-cut PPLN waveguide [107], (D) translational symmetry PPLN microring [108], and (E) rotational symmetry PPLN microring [109]. Reprinted with permission from [107–109]. © The Optical Society.

shape of a "comb" according to the desired periodically poled structure and then deposit these electrodes onto the surface of an LN thin film. After applying a static electric field with proper voltage and energization time to these electrodes, the periodic polarization structure is formed between the "combs" (Figure 14). For a Z-cut LNOI wafer, the electrode can be implemented via a conductive atom force microscope tip (Figure 14A). For detailed procedure of fabricating periodic structures on Z-cut and X-cut LN films, readers can refer to Gainutdinov et al. [110] and Mackwitz et al. [111].

Based on PPLN, we can fabricate PPLN ridge waveguide and microring by using etching [107–109] and other structures by using various fabrication methods as reviewed in Section 2.1.1, Manufacturing method. These PPLN-based structures open the door of exploring various nonlinear optical processes and their potential applications on an LNOI chip.

2.4 Optical coupling

Coupling light into and out of the chip is important to any LNOI chips. Well-designed, highly efficient coupler results in lower coupling loss and broader coupling bandwidth. Grating coupling and edge coupling are the two most widely used coupling methods in integrated LNOI photonics.

Grating coupling is well known for fiber-to-chip coupling [112, 113]. As shown in Figure 15A, a diffraction grating is patterned on the surface of an LNOI, through which light is coupled from a fiber above the chip to an on-chip LN waveguide. Grating coupling benefits from a simple fabrication process and flexible coupling position on the chip, but suffers from the limited bandwidth, high sensitivity to polarization state, and fiber alignment. The coupling efficiency is highly dependent on the incident angle θ, as shown in Figure 15A: the coupling efficiency decreases as the incident angle θ deviates from a specific value; the wavelength corresponding to the maximum coupling efficiency changes dramatically as the variation of the incident angle θ. Grating coupler's sensitivity to the fiber misalignment can be improved by optimizing design of the grating coupler [114]. To decrease power leaking to the substrate so as to increase the coupling efficiency, we can fabricate a Bragg mirror underneath the insulator layer, which adds an additional cost. Alternatively, the coupling efficiency can be increased by coating a silica layer on top of the nanostructure. The design principles of LNOI grating coupling are basically the same as those of SOI and other material platforms [112, 115].

Grating coupler cannot meet the requirement of all the integrated LNOI devices. The intrinsic operating mechanism of grating limits its operating bandwidth, making grating coupler incompatible with broadband devices, such as frequency combs. Moreover, grating coupler's sensitivity to polarization state and fiber alignment also restricts its application. To circumvent grating coupler's limitations, edge coupling or butt coupling is widely used in integrated LNOI photonics. As the name implies, edge coupler couples light from a lensed fiber to a waveguide whose cross section is in the plane of the end facet of the chip, Figure 15B. Lensed fiber can concentrate the mode profile in the fiber to a mode with mode field diameter ~2 μm and a working distance roughly the same (2 μm) [116]. To match such a mode field diameter, an inversed taper is designed at the edge of the chip to taper the width of a single-mode LNOI waveguide down to approximately 100 to 300 nm, providing a mode profile diameter ~1.6 μm. As a result, a good fiber-waveguide mode matching is achieved. The inversed taper also brings the benefit of matching the effective index of the waveguide to that of the fiber, minimizing back-reflection [117–119]. Edge coupling requires a good alignment of the fiber and the end facet of the chip, necessitating precise flexure stages and careful adjustment.

In the community of integrated LNOI photonics, grating coupling was used in some devices to achieve input and output coupling anywhere on the chip [120, 121].

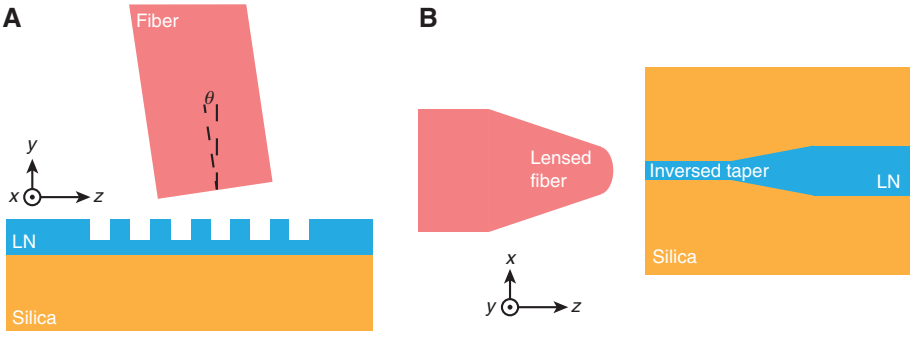

Figure 15: Schematic diagrams of optical coupling methods.
(A) Grating coupling, (B) edge coupling. Light propagates in $+z$ direction in the chip.

However, to increase operating bandwidth and reduce sensitivity to polarization state, edging coupling has achieved wider applications in various structures such as waveguides [49, 50, 55, 60], microring resonators [122], PPLN [123], and other structures [41, 54, 124]. By using a tapered lensed fiber, edge-coupling loss can be ~5 dB per facet [50] and can be further decreased to 1.7 dB per facet via an on-chip LN bilayer tapered mode size converter [125]. As for different LNOIs, +Z-cut LNOI shows a lower coupling loss than that of X-cut LNOI. And, MgO:LNOI shows a higher coupling loss than that of conventional LNOIs. In addition to the fiber and LNOI chip, alignment of the lensed fiber also affects the coupling loss. A detailed analysis of edge coupling in integrated LNOI photonics is given in Krasnokutska et al. [126].

Because of microdisk resonators' special structures, microdisk resonators can be directly coupled to a tapered fiber without any fiber-to-chip coupler. Coupling methods for microdisk are discussed in Section 2.2.1, Microdisk resonators.

3 Integrated devices

Section 2, Basic structures, reviews the essential building blocks for integrated LN photonic devices and systems. Based on these build blocks, we can achieve various functional devices on an LNOI platform, including modulators, optical switches, wavelength converters, frequency combs, polarization isolators, and entangled photon pair sources and quantum memories. This section discusses these devices in three categories: electro-optic devices, nonlinear optical devices, and optical frequency combs. For each category, this section introduces each device's operating mechanism, design principle and methodology, and performance metrics.

3.1 Electro-optic modulators

Lithium niobate is famous for its large second-order nonlinear coefficient $\chi^{(2)}$ and electro-optic coefficient r_{33}. Based on the electro-optic effect of LN, we can achieve various electro-optic devices, among which electro-optic modulator is the most widely used one. Based on the similar principle, optical switch can be realized.

Compared with the well-established integrated silicon modulators, the integrated LN electro-optic modulator has the unique advantage of changing the mode index via electro-optic effect instead of the plasma dispersion effect of silicon [127, 128]. Thus, LN modulator's response time to the modulation signal (on femtosecond timescales) is much shorter than that of silicon modulator (on nanosecond timescales), enabling an ultrahigh-speed modulation. In other words, high-speed LNOI electro-optic modulator is a traveling wave modulator, avoiding the long resistor-capacitance response time originated from the P-N junction of integrated silicon modulators [129].

Integrated electro-optic modulators are typically in the forms of waveguide phase modulator, MZI, and microring cavity intensity modulator [130], all of which can be efficiently realized based on LNOI [50, 55, 67, 131, 132]. Among the three different types of LNOI electro-optic modulators, MZI is the most frequently used one because of its simple operating mechanism, flexible design in meeting different metrics, and maximum utilization of r_{33} by choosing X-cut LNOI.

Traditionally, integrated LN electro-optic MZI modulators are fabricated by using titanium diffusion or proton exchange, resulting in weak field confinement and large mode volume. As a result, the metal electrodes have to be far apart from the optical waveguide in order to reduce the optical losses, inducing a high driven voltage [10, 133]. Recently, an integrated MZI modulator based on LNOI ridge waveguide is fabricated by using direct etching (Figure 16). Based on the strong field confinement and small mode volume provided by ridge waveguide, this modulator features a small spacing between electrodes and waveguide, leading to a CMOS-compatible drive voltage [50].

Electro-optic modulator is the key component in various optical systems, including optical communications, optical interconnects, and microwave photonics. Traditional LN modulator based on crystalline LN is a bulky discrete component, which is mostly suitable for fiber optical systems. Lithium niobate-on-insulator–based LN electro-optic modulator features CMOS-compatible driving voltage, high integration, broad modulation bandwidth, low optical loss, and good signal fidelity, thus enabling high-performance electro-optic modulation with seamless integration to CMOS [50]. Hence, LNOI-based LN electro-optic modulator has the potential to revolutionize optical communications, high-speed optical interconnects for data center and high-end computations, and integrated microwave photonics.

3.1.1 Design of electrodes

The most efficient way to achieve electro-optic modulation in an integrated LN waveguide is applying the microwave electric field along the direction of the largest electro-optic coefficient – r_{33}. As shown in Figure 16B, applying the driven voltage on one electrode, while grounding the other electrode,

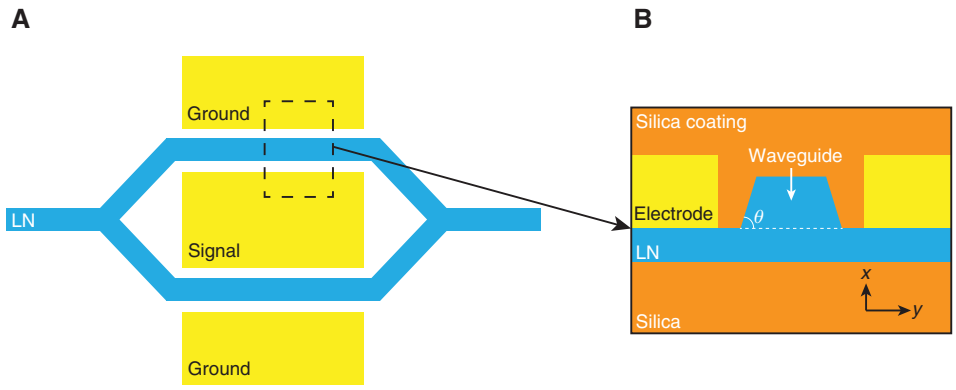

Figure 16: Schematic diagrams of an integrated LN MZI electro-optic modulator. (A) and (B) shows the top view and cross-section view, respectively.

can form a modulation electric field from the signal electrode to the ground electrode along *y* axis. This electric field passes through the X-cut LN ridge waveguide, thereby changing the mode index of the guided light traveling in the waveguide via the strong electro-optic coefficient r_{33} of LN.

Intensity of electro-optic effect depends on the intensity and spatial distribution of the optical and microwave fields and their overlap. Here, the optical and microwave fields are polarized in the same direction, for example, *y*-axis direction in Figure 16B. The optical field is well confined in the LN waveguide, which is guaranteed by the waveguide design in Section 2.1, Optical waveguide. Factors that may affect electro-optic coupling efficiency and DC feedback include waveguide width, etching depth (i.e. waveguide height), waveguide sidewall angle, and spacing between electrode and waveguide. When we determine the particular values of those factors, we usually meet trade-offs. For example, decreasing the spacing between electrodes and waveguide increases the microwave field strength in waveguide, but at the cost of increasing the propagation loss of the optical field (due to the ohmic loss of the electrode). A detailed theoretical discussion of realizing electro-optic effects in LN waveguide can be found in Honardoost et al. [43].

In the design of a high-speed traveling-wave modulator, we have to consider the radio-frequency (RF) transmission line's properties, among which the most important two are group velocity matching between RF and optical signals and impedance matching. In a traveling wave modulator, optical signal propagates within the optical waveguide, whereas the microwave signal propagates within the "microwave waveguide" (the coplanar waveguide, Figure 16B) at the same time. As shown in Figure 17, if group velocity of the optical signal does not match that of the microwave signal, optical signal may not be modulated by the same voltage along the waveguide in the modulation area. Such a velocity-mismatched electro-optic modulation may introduce phase error to the modulated optical signal, especially when the modulation frequency is high; that is, wavelength of the modulation signal is shorter than the electrode length [134].

To achieve a good group velocity matching, we have to ensure that the group refractive index of light is very close to that of microwave [43]. In conventional bulk LN modulator, group velocity matching is a challenging task due to the large difference between LN's dielectric constants in microwave (~28) and optical (~5) regimes [10]. To overcome such a large velocity mismatch between microwave and optical signals, LNOI modulator introduces a silica coating layer as superstrate and substrate of the waveguide (Figure 16B) [50, 67]. As a result, microwave field is mostly in the silica coating layer whose dielectric constant is ~4 in the microwave regime. Such a value is very close to the dielectric constant of LN in the optical regime (~5), simplifying group velocity matching significantly. Then, the thickness of the silica coating layer and width of the electrodes can be designed to achieve group velocity matching; that is, group refractive indices of microwave and light signals are very similar to each other.

Impedance matching is another important figure of merit (FOM) in designing a traveling wave modulator. When the microwave signal reaches the end of the coplanar waveguide, the ratio between the reflected electric field E_r and incident electric field E_i is defined by the reflection coefficient $\Gamma = E_r/E_i = (Z_L - Z_0)/(Z_L + Z_0)$, where Z_L is the impedance of the load, and Z_0 is the characteristic impedance of the coplanar waveguide (Figure 18). So, an impedance mismatching corresponds to a large reflected electric field, which will interfere with the modulation signal, forming a standing wave so as to introducing phase error to the modulated optical signal (Figure 18C). To achieve a good impedance matching, we have to design the coplanar waveguide so that its characteristic impedance matches the load impedance, which is usually 50 Ω [135].

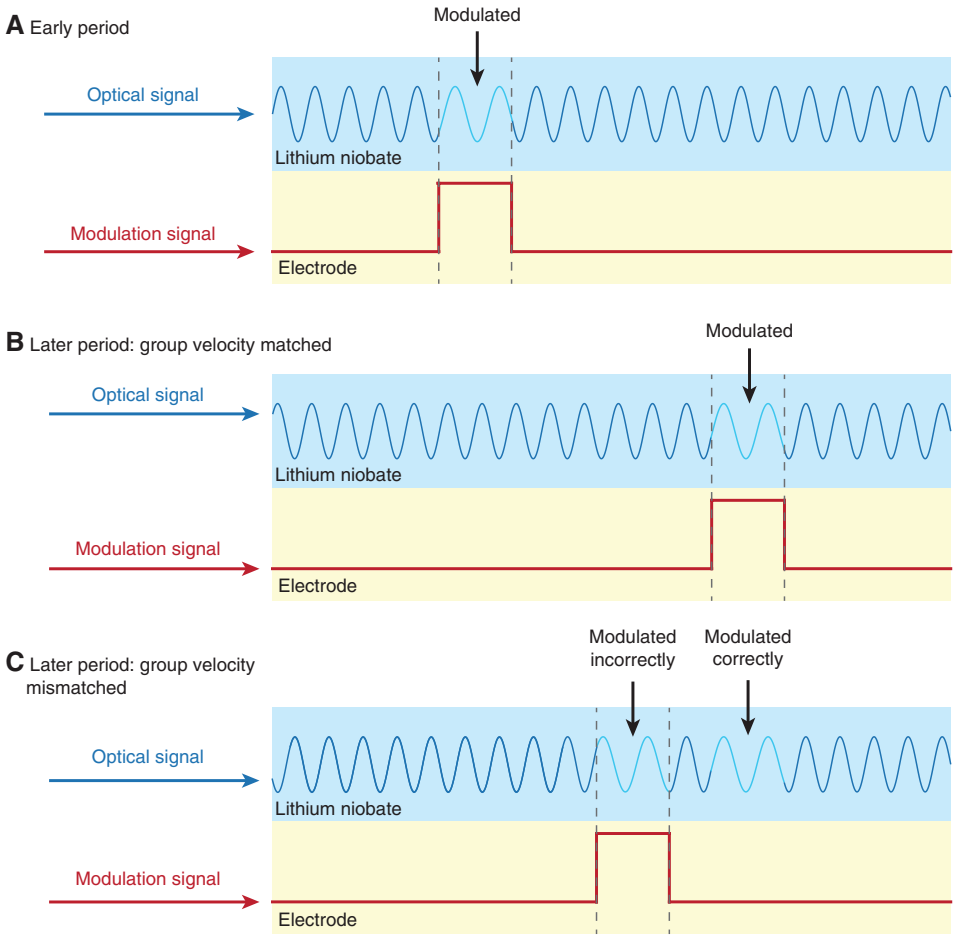

Figure 17: Schematic of group velocity matching of high-speed traveling-wave modulators.
(A) In early period, certain part of the optical signal is modulated by the microwave signal. (B) If group velocity of optical signal matches that of the microwave signal, optical signal will be modulated by the same electric field consistently, resulting in velocity-matched electro-optic modulation. (C) If group velocity of optical signal does not match that of the microwave signal, optical signal will not be modulated by the same electric field consistently. Such a velocity-mismatched electro-optic modulation may introduce phase error to the modulated optical signal, especially when modulation frequency is high; that is, wavelength of the modulation signal is shorter than the electrode length.

For a given modulation frequency, we can match the characteristic impedance of the coplanar waveguide Z_0 to the load impedance $Z_L = 50\ \Omega$ by engineering the thickness and width of the signal electrode (Figure 16). Theoretical results show that a thin electrode requires a wide signal electrode to match the impedance [67]. Furthermore, Z_0 decreases as the modulation frequency increases. To optimize the overall modulation frequency response of a traveling wave modulator, impedance matching can be combined with the microwave attenuation and microwave effective mode index as multiple figures of merit for the design of a coplanar waveguide [67].

Detailed design of an LNOI-based electro-optic modulator's waveguide and electrodes can be found in the supplementary information of He et al. [67]. A review shows a panoramic view of the design, fabrication, and performance of integrated LN modulator made by using titanium diffusion or proton exchange [39]. Design metrics and performance analysis in Rao and Fathpour [39] are applicable to the MZI modulators based on ridge waveguide, which is the focus of this review.

3.1.2 Metrics and performances

Many metrics, such as losses, extinction ratio, 3-dB bandwidth, and half-wave voltage, are being used to evaluate the performance of electro-optic modulators from different aspects.

The overall power losses due to the insertion of a modulator into an optical setup are the insertion loss. For example, compared with a single continuous fiber, a modulator coupled to the input and output fibers shows a higher loss – the insertion loss. Insertion loss includes the

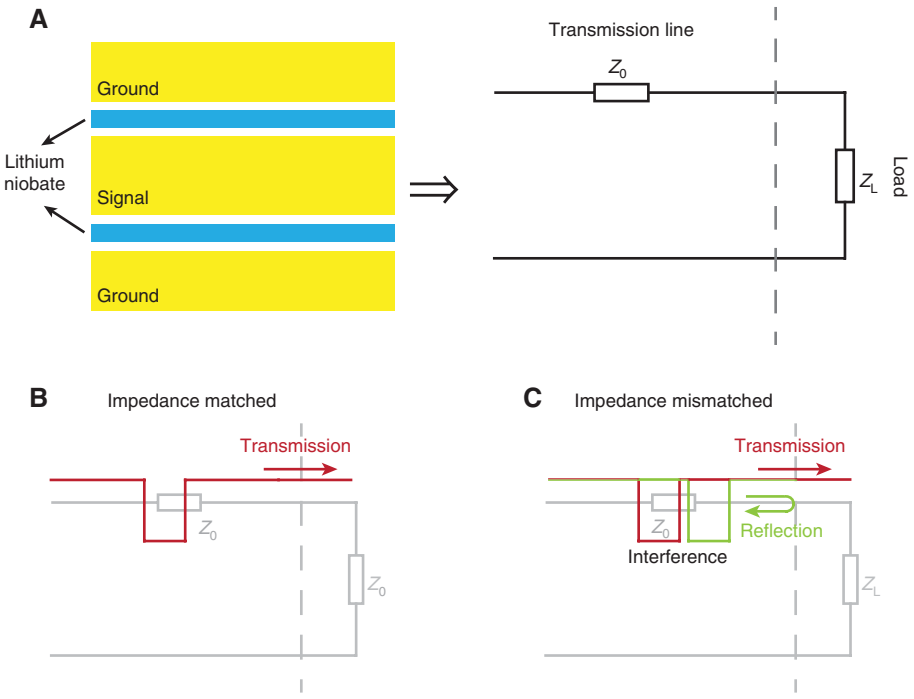

Figure 18: Schematic of impedance matching of traveling-wave modulators.
(A) Transmission-line model of the coplanar waveguide for microwave signal. (B) If impedance of the transmission line Z_0 matches the load impedance Z_L, the reflection will be minimized. (C) If the impedance of the transmission line mismatches the load impedance, part of the microwave signal will be reflected back to the transmission line. Such a reflected wave will interfere with the modulation microwave signal, leading to a standing wave and bringing phase error to the modulated optical signal.

interchip coupling loss and intrachip propagation loss. Coupling loss and different coupling methods have been reviewed in Section 2.4, Optical coupling. Propagation loss of an electro-optic modulator includes not only the propagation loss of LNOI waveguides (Section 2.1.3, Propagation loss), but also the Ohmic loss due to the metallic electrodes. Ohmic loss can be decreased by enhancing the optical confinement or increasing the waveguide-electrode spacing. An MZI modulator shows an overall intrachip propagation loss of 0.5 dB (0.03 dB/cm) with a coupling loss of ~5 dB per facet (edge coupling as Figure 15B) [50]. Another hybrid silicon and LN MZI modulator shows an insertion loss of 2.5 dB with a propagation loss of 0.3 dB/cm [67].

Extinction ratio is defined by the ratio between the intensity of outputs of a modulator with and without the microwave signal. Ideally, extinction ratio should reach infinite. In practice, however, following either of two facts can result in a finite extinction ratio. First, fabrication imperfections may induce that the waveguide beam splitter deviates from the ideal 50:50 split ratio [136]. Second, various reasons, such as fabrication imperfections and different amplitudes of microwave electric field across the two arms, may lead to a certain degree of imbalance between the two arms of MZI, whose optical path length does not correspond to an integer times of 2π [50, 136]. A ridge-waveguide MZI-based modulator made by RIE reaches an extinction ratio of 10 dB [55], which has been further improved to 30 dB [50]. An even higher extinction ratio up to 53 dB can be achieved based on a cascaded MZI design [137].

Half-wave voltage (V_π) corresponds to voltage required to induce a π phase difference between the two arms of an MZI electro-optic modulator, shifting the optical output from maximum to minimum. Because V_π is inversely proportional to the length of the microwave electrode L, there is a design trade-off between V_π and L. A shorter modulator has a higher integration level, whereas a longer modulator can achieve a lower V_π [43]. For the state-of-the-art integrated LN MZI modulator, a modulator with $L = 20$ mm shows a V_π of 1.4 V, whereas a smaller footprint of $L = 5$ mm requires a higher V_π of 4.4 V [50].

Modulation bandwidth is a key metric to evaluating high-speed modulation. For a given electro-optic modulator, as the microwave frequency increases, the effect of impedance matching, group velocity matching, and RF attenuation increases. As a result, transmission of the modulator decreases as the microwave frequency increases [43]. The modulation bandwidth is usually

quantified by the microwave frequency at which the transmission is 3 dB lower than that at DC: the 3-dB bandwidth. A shorter microwave electrode (smaller L) induces a larger 3-dB bandwidth and a higher V_π, resulting in a voltage-bandwidth trade-off [138], as shown in Figure 19. The state-of-the-art integrated LN modulator can strongly confine the optical mode within the waveguide while keeping the microwave mode within the silica coating area (refractive index of LN in optical regime is similar to that of silica in microwave regime), so as to match the microwave and optical group velocities at high microwave frequencies with a slightly worse electro-optic overlap. Such modulators can achieve a voltage-bandwidth performance of V_π = ~1.4 V and 3-dB bandwidth over 45 GHz with L = 20 mm [50]. Another hybrid silicon and LN MZI modulator achieve a 3-dB bandwidth at least 70 GHz,

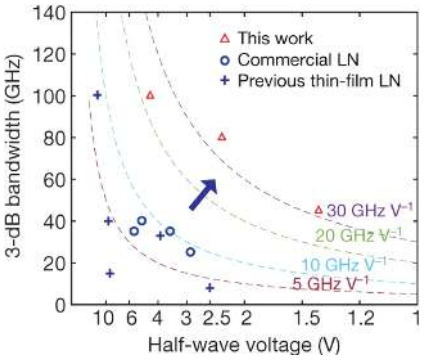

Figure 19: The voltage-bandwidth trade-off of LNOI modulator. "This work" refers to Wang et al. [50]. Reprinted by permission from Wang et al. [50], Springer Nature Limited, copyright 2019.

half-wave voltages V_π of 5.1 and 7.4 V with the modulation lengths L of 5 and 3 mm, respectively, and an insertion loss of 2.5 dB [67] (Figure 20).

3.1.3 Other types of modulators

In addition to LNOI-based electro-optic MZI modulators, many other types of intensity or phase modulators can also be achieved on LNOI platform.

Microring modulator is one kind of intensity modulator, which changes its resonant wavelength by varying the mode index of the light traveling within the ring based on the electro-optical effect [139, 140]. Consequently, intensity of the input CW light experiences different transmission coefficient under different modulation voltage, achieving intensity modulation. Depending on the electrode design, either X-cut or Z-cut LN thin films can be used to fabricate microring modulators. Considering the working principle of microring modulators, the metric used to evaluate its performance is electro-optic modulation coefficient, which is defined by the shift in the resonant wavelength when a certain driving voltage is applied.

A ridge-waveguide microring modulator consisted of Z-cut LN thin film sandwiched by electrodes at the top and bottom. Such a modulator with a ring diameter 200 μm achieved a Q factor of 4×10^3, propagation loss of 4 dB/cm, and a modulation coefficient of 1.05 pm/V [25]. A racetrack microring modulator demonstrated a modulation coefficient as high as 7 pm/V [55]. A microring modulator based on a hybrid silicon and Z-cut LN thin-film platform

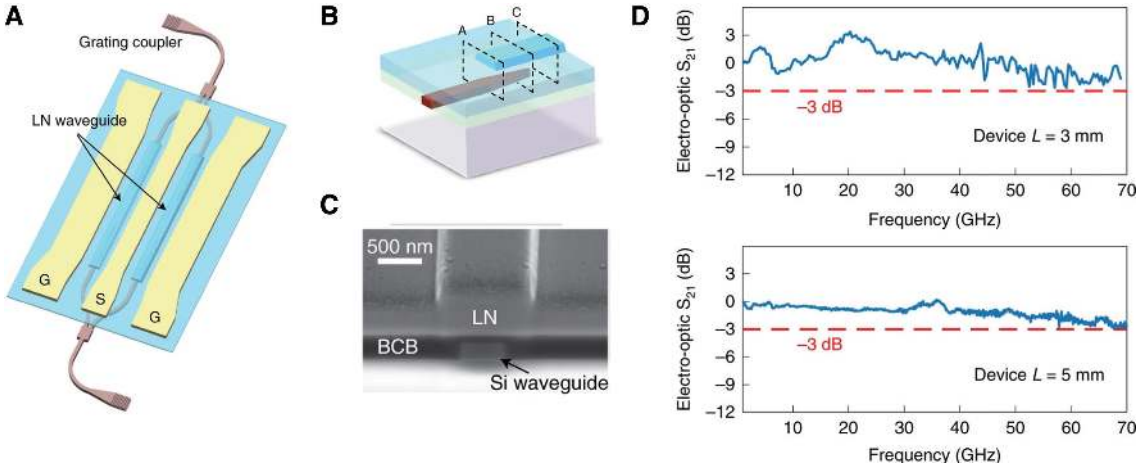

Figure 20: Hybrid silicon and LN MZI modulator.
(A) Schematic diagram of the modulator. (B) Schematic diagram of the Si-LN waveguide coupler. (C) Scanning electron microscope image of the cross section of the coupler. (D) Electro-optic response of the modulator with different device lengths. Reprinted by permission from He et al. [67], Springer Nature Limited, copyright 2019.

achieved a modulation coefficient of 1.7 pm/V [141] and was further improved to 12.5 pm/V by using an optically transparent electrode [28]. A microdisk modulator demonstrates a modulation coefficient of 3.0 GHz/V (24 pm/V) [51]. Such a microdisk modulator can show an unloaded Q as high as 1.19×10^6. Another modulator with a novel structure – nested racetrack dual microring – achieves a modulation coefficient up to 52.6 pm/V [142].

To summarize the discussion on microring modulators, we compare its performance with that of MZI modulators. The typical diameter of microring modulators is tens of micrometers, which is much smaller than the length of MZI modulators (a few millimeters to several centimeters). Two typical microring modulators show 3-dB bandwidths of 5 and 30 GHz with the corresponding extinction ratios of 4 and 3 dB, respectively [51, 55]. Thus, the 3-dB bandwidth and extinction ratio of microring modulator are much lower than those of MZI modulators (bandwidth >70 GHz with the corresponding extinction ratio of 30 dB [50]).

In addition to MZI and microring, intensity modulation can also be achieved based on a single multimode waveguide. Such a modulator couples the fundamental TE_0 mode and TE_1 mode into a multimode waveguide and modulates those two modes via the electrodes along the waveguide. Those two modes have different mode refractive indices so that they accumulate different phases along the waveguide in the modulation area. After modulation, TE_1 mode is converted to TE_0 mode and then interfere with the other mode [143], similar to MZI modulators, as shown in Figure 21A. Although the multimode waveguide modulator is demonstrated based on SOI, the concept can be simply adopted to LNOI by directly modulating a multimode ridge waveguide via the electro-optic effect.

Intensity modulation can also be achieved via grating coupling modulators. As shown in Figure 21B, when applying voltage to the interdigital electrode, a grating is formed via the change of refractive indices of the channel waveguide's certain segments closing to the electrodes. So, light guided in the waveguide can be redirected to the substrate, reducing the output light effectively. Based on this mechanism, an intensity modulator can be realized when microwave signal is applied [144]. Although the grating coupling modulator is demonstrated based on a channel waveguide made by proton exchange, the concept can be simply adopted to LNOI by directly modulating a ridge waveguide.

Other than the intensity modulators, phase modulators have also been demonstrated based on LNOI. Phase modulator can be realized by applying microwave signal across the LNOI-based ridge waveguide via electrodes along the waveguide. Design methods of waveguides and electrodes, respectively, can be found in Sections 2.1, Optical waveguide, and 3.1.1, Design of electrodes. An integrated LNOI phase modulator is demonstrated with low half-wave voltage ($V(\pi)$) (3.5–4.5 V with 2-cm length) and low on-chip loss (~1 dB) [132]. Such a phase modulator can be used to generate a frequency comb with 10-nm spanning. This phase modulator's modulation bandwidth is limited by the relatively large optical loss induced by the waveguide's Fabry–Pérot cavity effect [132].

3.2 Nonlinear optics

In addition to the electro-optic effect, LN is also used to achieve many other second-order nonlinear processes including SHG, SFG, DFG, and optical rectification

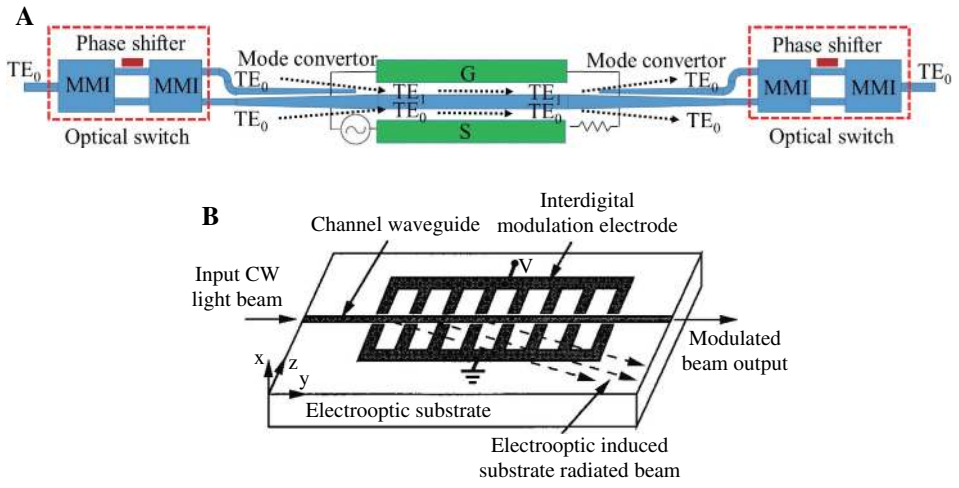

Figure 21: Multimode waveguide modulator and grating coupling modulator.
(A) Schematic view of a multimode waveguide modulator. Reprint from Zhou et al. [143], with the permission of the authors. (B) Schematic view of a grating coupling modulator. Reprinted from Wang et al. [144], with the permission of AIP Publishing.

[145]. And, based on LN's large third-order nonlinearity ($\chi^{(3)} = 1.6 \times 10^{-21}$ m^2 V^{-2}), LN can be used to realize many third-order nonlinear processes including third-harmonic generation (THG), four-wave mixing (FWM), Kerr effect, Raman scattering [146], and self-focusing [145]. By combining LN's second- and third-order nonlinearities, we can first generate nonlinear signal and then manipulate it via electro-optic effect [92]. So far, second-order nonlinear processes are still the major applications of LNOI in nonlinear optics.

3.2.1 Second-harmonic generation

Second-harmonic generation is the most common and well-developed nonlinear process of integrated LNOI photonic devices [147]. According to a similar principle, SFG and DFG can also be achieved based on the strong second-order nonlinearity $\chi^{(2)}$ of LN.

Second-harmonic generation can be achieved in an LNOI microdisk cavity via noncritical direct phase matching [148–150]. An integrated LNOI microdisk resonator achieved an SHG conversion efficiency of 0.109 W^{-1} [78], which is similar or even better than that demonstrated by microdisks made from other materials including silicon, silicon nitride, and GaAs [151–153].

The SHG conversion efficiency of microdisk resonators is restricted due to microdisk's limited design flexibilities and the high loss of WGM of second-harmonic signal. On the other hand, PPLN can show a much better performance in SHG considering PPLN's particular design for quasi–phase matching (Section 2.3, Periodically poled LN structures). Based on a PPLN made by annealed and reverse proton exchange, a high normalized conversion efficiency up to 150%/W cm^2 was realized for SHG in the 1550-nm band [96]. Mg-doped or MgO-doped LN is used to form PPLN (called PPMgLN or PPMgOLN) for blue or UV light generation via SHG [154]. A rib-loaded waveguide consisting of an SiN ridge on top of a PPLN thin film showed a high efficiency up to 160%/W cm^2 for SHG with pump at 2 μm [64]. Based on a nanostructured PPLN ridge waveguide, an ultrahigh normalized efficiency of 2600%/W cm^2 was demonstrated for SHG with pump around 1.5 μm [107]. In this work, the PPLN is first fabricated based on an MgO-doped LNOI, and then the ridge waveguide was achieved by patterning PPLN using EBL and dry etching (Figure 14C). To further increase the nonlinear conversion efficiency, microring resonator was fabricated on LNOI-based PPLN (Figure 14D). Such a microring shows a Q factor up to a million and achieves SHG with a normalized conversion efficiency of 9×10^{-4} mW^{-1} [108]. Moreover, a dual-resonant PPLN microring is realized for quasi-phase matched SHG (Figure 14E). Such a PPLN microring shows a critically coupled pump mode with a load Q factor of 8×10^5 and an overcoupled second harmonic mode with a loaded Q factor of 1.5×10^5. As a result, this PPLN microring demonstrates an SHG efficiency as high as 250,000%/W – the state-of-the-art value provided by integrated photonics platforms [109]. Quasi–phase matching of PPLN always suffers from limited bandwidth. By carefully designing the waveguide for a smaller dispersion (which is well known as dispersion engineering), the effective bandwidth of the pump of SHG realized by PPLN waveguide can be improved by more than one order of magnitude [155]. This is essential to improve the performance of PPLN-based devices such as PPLN-based frequency combs.

As an alternative of PPLN, which changes material properties to form the periodicity required by quasi–phase-matching condition, we can pattern LN or its coating material to meet the phase-matching condition. By directly etching LNOI, periodically grooved LN can meet the quasi–phase-matching condition and achieve a conversion efficiency as high as 41%/W cm^2 [54]. Gradient metasurface consisting of arrays of silicon phased antennas on top of an LN ridge waveguide enables the phase matching–free SHG over a wide pump wavelength range [124].

In addition to microdisk and PPLN, other LNOI structures have also been used to achieve SHG. Based on the strong thermo-optic birefringence of LN, thermally tuned type I intermodal phase matching is demonstrated in LNOI ridge waveguides. Such a device can achieve SHG with a large wavelength tuning (tuning slope of 0.84 nm/K) and a conversion efficiency of 22.2%/W cm^2 [156]. An LNOI-based photonic crystal nanobeam cavity demonstrates SHG with a conversion efficiency ~4×10^{-9}/mV [90] (Section 2.2.3, Photonic crystal nanocavities).

3.2.2 Other nonlinear processes

Lithium niobate's strong second- and third-order nonlinearities enable several nonlinear processes, including SFG, DFG, THG, and FWM [157]. As an example, Ye et al. [158] demonstrated an SFG process in a microdisk cavity via modal phase matching whose conversion efficiency reaches 2.22×1010^{-6} mW^{-1}. By cascading those nonlinear processes, such as generating a third-harmonic signal by SFG between a second-harmonic wave and a fundamental wave (Figure 22A [159]), we can either electrically manipulate nonlinear conversion processes or achieve nonlinear

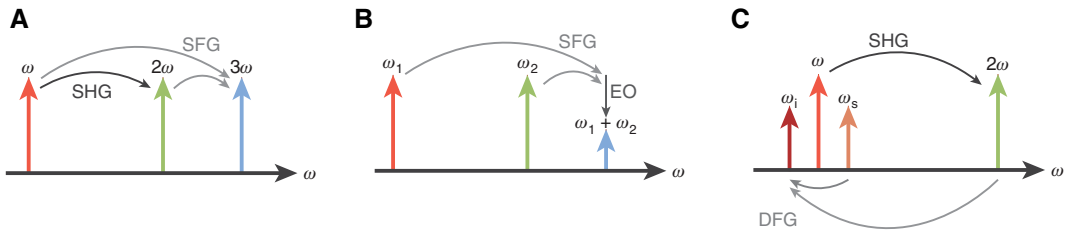

Figure 22: Cascaded nonlinear processes based on integrated LNOI photonics.
(A) Cascading SHG and SFG processes generates a third harmonic wave. (B) Cascading SFG and electro-optic processes enables modulating the sum-frequency wave electrically. (C) Cascading SHG and DFG processes generates a signal wave and an idler wave around the fundamental wave frequency.

responses, which cannot be generated by conventional nonlinear processes. This cascaded SFG process was recently realized via an LNOI microdisk resonator for the first time [160]. Moreover, based on the broadband quasi–phase matching in an X-cut LN microdisk, we can simultaneously generate second-harmonic and cascaded third-harmonic waves with normalized conversion efficiencies as high as 9.9%/mW and 1.05%/mW^2, respectively, as a consequence of using the highest nonlinear coefficient d_{33} of LN [73].

Based on a PPLN on insulator ridge waveguide covered with electrode, we can modulate the intensity of quasi-phase matched SFG via electro-optic polarization coupling according to the cascaded SFG and electro-optic polarization coupling process; that is, the cascaded sum-harmonic wave is generated via a cascaded process by an SFG between the electro-optic modulated and pump waves (Figure 22B). The strong light confinement and large mode overlapping provided by the ridge waveguide effectively reduce the driving voltage and pump power [161]. Furthermore, an effective FWM is demonstrated in an LNOI microdisk via cascaded quadratic processes of SHG and DFG in the telecom band. The idler wave is generated via a DFG between a signal wave and a second-harmonic wave, which is generated from the fundamental wave via SHG (Figure 22C) [80].

Theoretical results show that gradient metasurface (Section 3.2.1, Second-harmonic generation) can upconvert light from 3.4 to 1.064 μm with a pump at 1.55 μm via SFG [162].

Stimulated Raman scattering (SRS) is an important third-order nonlinear process. Based on the $\chi^{(3)}$ nonlinearity of LN, SRS has been demonstrated in LN crystal [163] and LNOI microdisks [146]. Lithium niobate-on-insulator microdisk shows a high pump-to-strokes efficiency of 0.46. In addition to SRS, other third-order nonlinear processes could also be realized based on LNOI devices; more details can be found in Section 5.1, High-performance nonlinear and quantum optics.

3.3 Optical frequency comb

Optical frequency comb is a spectrum consisting of phase-coherent equally spaced narrow lines. Since frequency comb was first used as a precise ruler in the spectral domain [164], frequency comb has shown various applications including atomic clocks, distance measurements, and dual-comb spectroscopy. As the first realization of frequency comb, mode-lock laser may not be suitable for on-chip applications because of the challenges of miniaturization. Frequency comb can be realized on a photonic chip based on Kerr nonlinearity of microcavity [165, 166], cascaded second-order nonlinear processes in PPLN ring [167], and electro-optic modulation [84].

Lithium niobate's record-high second-order nonlinearity $\chi^{(2)}_{zzz}$ makes it the ideal material platform for achieving second-order nonlinear comb (based on d_{33}) and electro-optic comb (based on r_{33}). Based on the quasi–phase matching provided by a PPLN microring, cascaded SHG and parametric downconversion process can realize a frequency comb, as predicted by the theoretical analysis [167]. On the other hand, we can generate optical frequency comb on LNOI by electro-optically modulating the phase of an optical signal via a microwave signal. Input of such an electro-optic comb is usually a CW light, which, after the phase modulation, becomes a spectrum consisting of many equally spaced sidebands whose spacing (so-called repetition rate) is determined by the frequency of the microwave signal [168].

Microring resonators and racetrack resonators are frequently used to realize an LNOI electro-optic comb. Lithium niobate ridge waveguide provides a strong confinement of light, effectively reducing the waveguide-electrode spacing, leading to a low half-wave voltage V_π, resulting in a strong phase modulation index $\beta = (V_p/V_\pi)$. Furthermore, the high Q factor of these resonators results in a low round-trip power loss. The strong phase modulation combined with the high Q factor gives a flat and broad

comb with many comb lines. Lithium niobate-on-insulator electro-optic comb's repetition rate is determined by the resonator design and the modulation frequency: the optical sidebands generated by the phase modulation are resonant when the modulation frequency is integer times of the free spectral range of the resonator. A unique advantage of electro-optic comb is that the repetition rate can be tuned rapidly by changing the modulation frequency. A racetrack resonator optical frequency comb shown in Figure 23 depicts a comb bandwidth greater than 80 nm and more than 900 comb lines with optical input at 1550 nm and repetition rate around 10 GHz [84]. This comb can show a comb spectrum greater than 20 nm even under a 30-MHz modulation frequency detuning from the free spectral range of the resonator. Moreover, this comb can generate beat notes with arbitrary repetition rate by adding two phase-locked microwave signals to the electrodes.

On the other hand, based on a single-crystalline LN microdisk resonator in a copper microwave cavity, a resonant electro-optic frequency comb can be realized by using microwave field to phase-modulate the light via the Pockels effect [169]. Such a resonant electro-optic frequency comb can generate a comb spectrum spanning ~11 nm (~1.6 THz) with more than 180 comb lines by using a microwave power as low as 20 dBm. Such a low microwave power is a result of the resonant enhancement provided by the microwave cavity. This comb also features a high phase stability due to the fixed interaction of the stabilized microwave and optical sources.

Based on the third-order nonlinearity of several material platforms, such as silica and silicon nitride, integrated Kerr frequency combs achieved fast development recently [165, 170, 171]. However, these Kerr combs still meet the challenge in integrating with other functional devices, such as filter and modulator, limiting the system-level integration. The large third-order ($\chi^{(3)}$) and second-order ($\chi^{(2)}$) nonlinearities of LN enable monolithic integration of Kerr frequency combs with other functional devices on the same chip. For example, Wang et al. [92] realized monolithic LN photonic circuits consisting of a broadband Kerr frequency comb (more than two-thirds of an octave, $\chi^{(3)}$), an electro-optically tunable add-drop filter ($\chi^{(2)}$), and a modulator ($\chi^{(2)}$). To achieve Kerr frequency combs effectively, we need to design a microring resonator with both a high Q factor and a broadband anomalous dispersion. The high Q factor guarantees that the cascaded FWM process can overcome the optical loss of the microring. The anomalous dispersion compensates the self- and cross-phase modulations, that is, nonlinear response as a result of the high-intensity pump [172]. Such a microring resonator can be designed by carefully engineering the dispersion of an LNOI ridge waveguide.

As an alternative to resonator-based comb, we can also achieve LNOI electro-optic frequency comb by directly modulating the phase of optical signal via electrodes along an optical waveguide commercialized crystalline LN phase modulator, which can be used to generate electro-optic frequency comb based on fiber optical systems [173]. Recently, integrated LN waveguide–based

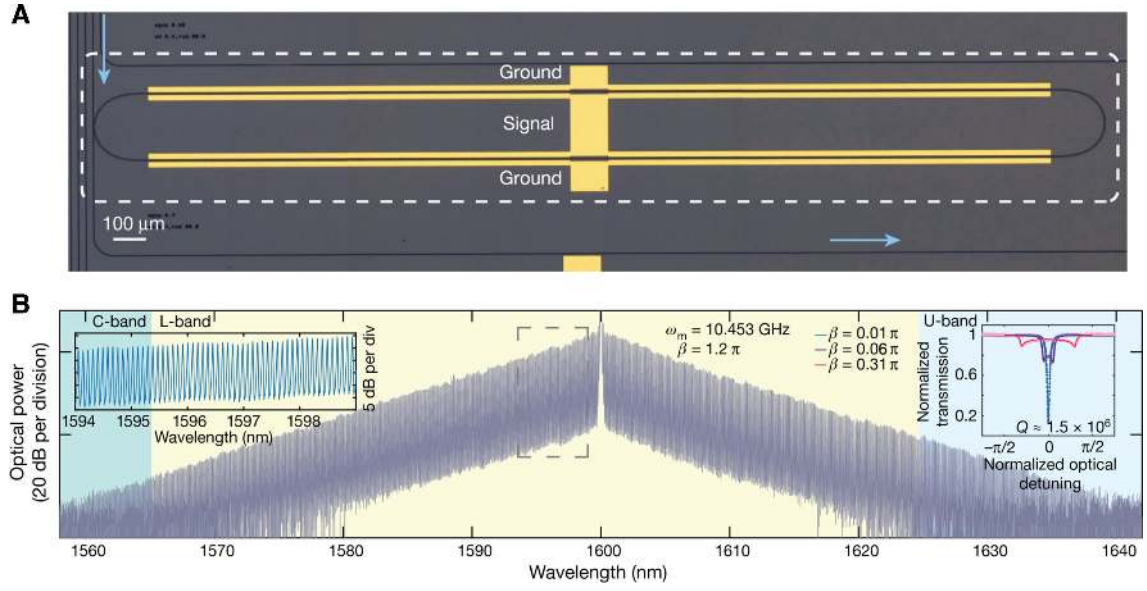

Figure 23: Broadband electro-optic frequency comb generation in a lithium niobate microring resonator.
(A) SEM diagram of a lithium niobate microring resonator. (B) Ultra broadband frequency comb spectrum. Reprinted by permission from Zhang et al. [84], Springer Nature Limited, copyright 2019.

frequency comb with more than 40 sidebands and large spectral range has also been demonstrated [132]. Different from resonator-based frequency comb whose repetition rate has to be a harmonic of the resonator's free spectral range, waveguide-based nonresonant comb can tune the repetition rate to any frequency, which equals the modulation frequency. Because waveguide-based comb's phase-modulation length is shorter than that of resonator-based comb, waveguide-based comb shows a narrower bandwidth and a smaller number of comb lines. Electro-optic phase modulator-based combs can be used in dual-comb spectroscopy [174] and quantum optics [175]. Although those applications are demonstrated by using discrete phase modulators, the concept can be implemented by using LNOI waveguide–based nonresonant combs to miniaturize the systems.

4 Systems and applications

The excellent performance of integrated LNOI devices not only can improve the system-level performance of LN's traditional applications in optical communications, microwave photonics, and quantum optics, but also can enable many new applications, such as optical computing [42] and metrology. Moreover, integrated LNOI photonics provides a versatile platform to miniaturizing various devices such as modulators, nonlinear devices, frequency combs, and quantum optic devices onto a photonic chip [42, 176]. In this section, we discuss recently demonstrated applications of integrated LNOI devices and their potential applications in the future.

4.1 Optical communications and data center

Based on the low-loss broadband channel provided by optical fiber, optical communications has been widely used to transmit information to remote end by using light to carry signal [177]. In addition to the long-haul communications based on optical fiber, optical communications is also being used in machine-to-machine, board-to-board, interchip, and intrachip communications, especially in data centers, which have been blooming along with the fast development of artificial intelligence and cloud computing [178].

In optical communications, electro-optic modulator is a key component that transfers the information from electric domain to the optical domain. Such a modulation is realized by varying an optical signal's amplitude, or frequency, or phase based on an electric signal carrying the information [177]. To achieve effective and reliable communications, an optical communication system needs to meet many performance metrics, several of which are highly related to the modulator's performance. Data transmission rate is the number of data that are transmitted per unit time. Extinction ratio is the ratio of the energy for transmitting a logic level "1" to that for transmitting a logic level "0." Long-haul optical communications typically require an extinction ratio greater than 20 dB to guarantee the signal fidelity [39]. Bit error ratio (BER) is the ratio of the number of incorrect bits to the number of total bits received in a transmission. A modulated signal with a BER lower than 10^{-3} can meet the requirement of long-haul optical communication [179].

So far, electro-modulations in optical communications could be realized based on several platforms, including silicon, polymer, indium phosphide, and plasmonics [6, 180–185]. While each of these platforms can feature certain excellent performance metrics, such as high data transmission rate and low drive voltage provided by polymer, none of these materials can meet all the performance metrics required by modern optical communications simultaneously. By combining the excellent electro-optical properties of LN as well as the fabrication techniques for LNOI and ridge waveguide, the integrated LNOI electro-optic modulator can meet all performance metrics required by modern optical communications. For example, an integrated LNOI electro-optic modulator can achieve a data transmission rate of 70 Gbaud, an extinction ratio of 30 dB, an on-chip loss of less than 0.5 dB, and a BER of less than 10^{-6} under a CMOS-compatible driving voltage ~200 mV [50]. Another hybrid silicon and LN electro-optic modulator features a data transmission rate of 56 Gbaud, an extinction ratio greater than 40 dB, an insertion loss of 2.5 dB, a BER of less than 3.8×10^{-3}, and a voltage–length product of 2.2 V cm [67].

Past decades have witnessed the rapid development of the society driven by information technology, among which data center is the key facility for processing, distributing, and storing data. The performance and cost of data centers are highly dependent on the data exchange and distribution via the integrated optoelectronic system. Such a system's most important component is the electro-optic modulators, which determine the overall speed and power consumption of intra–data-center communications.

For the applications in data center, the most important metrics of an electro-optic modulator are bandwidth, power consumption, size, and cost [186]. The increasing data volume requires high-speed modulation. Meanwhile, system integration and cost-effectiveness necessitate

the CMOS compatibility of a modulator, especially the modulator's CMOS-compatible drive voltage. As a competitive candidate in meeting all those metrics, an LNOI electro-optic modulator demonstrates data transmission of 70 Gbaud (2-ASK), a driven voltage of 200 mV, a 20-mm electrode length, and a bit error rate of less than 1×10^{-6} [50]. Because data-center applications require a relatively low extinction ratio, ~3.5 dB [187], modulation bandwidth of this LNOI electro-optic modulator can be further increased by scarifying the extinction ratio. In terms of the overall performance, this LNOI electro-optic modulator has taken a big step toward the goal of high-performance integrated electro-optic modulation. Such a modulator has the potential to achieve broad applications in data centers including direct driving serializer/deserializer and dense wavelength-division-multiplexing optical systems.

4.2 Integrated microwave photonics

Integrated microwave photonics is an emerging area aiming at generating, transforming, modulating, and detecting microwave signal based on integrated optical devices. A typical integrated microwave photonic system encodes microwave signal onto light wave and then transmit and process the microwave modulated optical signal on a photonic chip and finally convert the processed sidebands to microwave domain. Advantages of integrated microwave photonics over RF integrated circuits include broader bandwidth, lower energy consumption, smaller footprint, and less sensitivity to electromagnetic interference. [188]. Heterogeneous integration with different materials has been tried to boost the performance of integrated microwave photonic devices. Some of these devices can achieve better performance by treating LNOI and ridge waveguide as platform.

In integrated microwave photonic systems, electro-optic modulator is the key device to encode RF signal into optical domain [188]. Because of LN's extraordinary performance, excellent stability, linearity, and high-power handling ability, LN has been used as bulk electro-optic modulators for decades [10]. By taking advantage of the high index contrast provided by LNOI ridge waveguide, integrated LN modulator is a very promising choice for integrated microwave photonics. Integrated LN modulator features a broad bandwidth, CMOS-compatible modulation voltage, and low propagation loss, enabling high-performance modulation on single LNOI chip [39, 50, 67].

Optical frequency comb has been widely used in integrated microwave photonics to achieve various functional devices including sources and filters [171]. Microwave signals can be obtained by using a high-speed photodetector to detect the beat note generated by a Kerr frequency comb [189]. The generated RF frequency corresponding to the comb's repetition rate can show a very low noise because the noise of the optical source is divided by the ratio of the optical to beat-note frequencies. In addition to microwave source, a programmable single-passband microwave filter can also be achieved based on a Kerr frequency comb [190]. Although these microwave photonic devices are not demonstrated based on LNOI-based frequency combs, the principles can be implemented based on LNOI-based Kerr combs or electro-optic combs as reviewed in Section 3.3, Optical frequency comb.

4.3 Quantum optics

The second-order nonlinear processes provided by LN include not only SHG, SFG, and DFG, but also spontaneous parametric downconversion (SPDC), which gives rise to various applications in quantum optics, including entangled photon pair generation and quantum memory. These topics were reviewed comprehensively in Alibart et al. [191]. At the time of this review, lots of waveguides are still fabricated by titanium diffusion and proton exchange, limiting the performance of integrated LNOI quantum photonics.

Basic structures for implementing nonlinear optical processes for quantum optics are the same as those for regular nonlinear optical processes, such as PPLN, power splitter, wavelength multiplexer and demultiplexer, and phase modulator [192]. In principle, all these waveguide-based structures can be implemented by LNOI ridge waveguide, leading to a much better performance than those based on titanium-diffused or proton-exchanged waveguides. And, the underlying physics of these nonlinear optical devices can be explained by using quantum approaches [191], building the foundation for quantum optical applications.

Based on the parametric downconversion in an MgO:LNOI microdisk, quantum correlation between the signal and idler beams was achieved; that is, the variance of the signal and idler photocurrent difference fluctuation is below the short noise limit [193]. Furthermore, either signal or idler beam alone can show intensity squeezing; that is, the noise of intensity of either signal or idler beam is below the short noise limit. Such an MgO:LNOI microdisk can be used as an efficient single photon source with narrow bandwidth.

Entangled photon pair source is the essential component for various quantum applications including quantum

communication [103], computation, and metrology. Entangled photon pair can be efficiently generated via the SPDC in PPLN waveguide. Energy-time and time-bin entangled photon pairs can be generated via the SPDC in a PPLN waveguide with a high conversion efficiency ~10^{-6} [194]. Based on a type II quasi-phase matched PPLN ridge waveguide, photon pairs with full width at half maximum of 1 nm and brightness of ~6×10^{-5}/s/GHz can be generated [195]. By integrating LN waveguide circuits and PPLN on a chip, we can achieve the quantum interference of two pairs of entangled photons, whose phase can be controlled by an electro-optic modulator (Figure 24) [196]. Such an LN circuit enables on-chip engineering of quantum light sources.

Single-photon detector is an essential component in quantum optics with applications in proof-of-concept experiments [197], quantum computing [198], and quantum communications [199]. Traditional LN integrated quantum optics systems use fiber to couple photons out of the chip to the single-photon detector. Such a detecting method suffers from the positioning of the fiber. To eliminate this drawback, an integrated transition edge sensor on titanium-diffused LN waveguides is demonstrated [200]. Transition edge sensor operates with the stage between a superconductive state and resistance state, which changes according to the temperature shift caused by single-photon absorption. Such a sensor detects light by coupling the evanescent field decaying away from the LN waveguide to an on-chip detector. Transition edge sensor can work at different frequencies and is suitable for broadband detection [201]. Transition edge sensor opens the door of integrating an entire quantum optics system including entangled photon pair source, photon manipulation, and single-photon detector onto a single LNOI chip.

Quantum memory is a vital component of quantum computing systems and quantum information processing systems. Lithium niobate waveguides doped with erbium and thulium can store quantum optic information for the time scale of nanosecond and microsecond [42, 202].

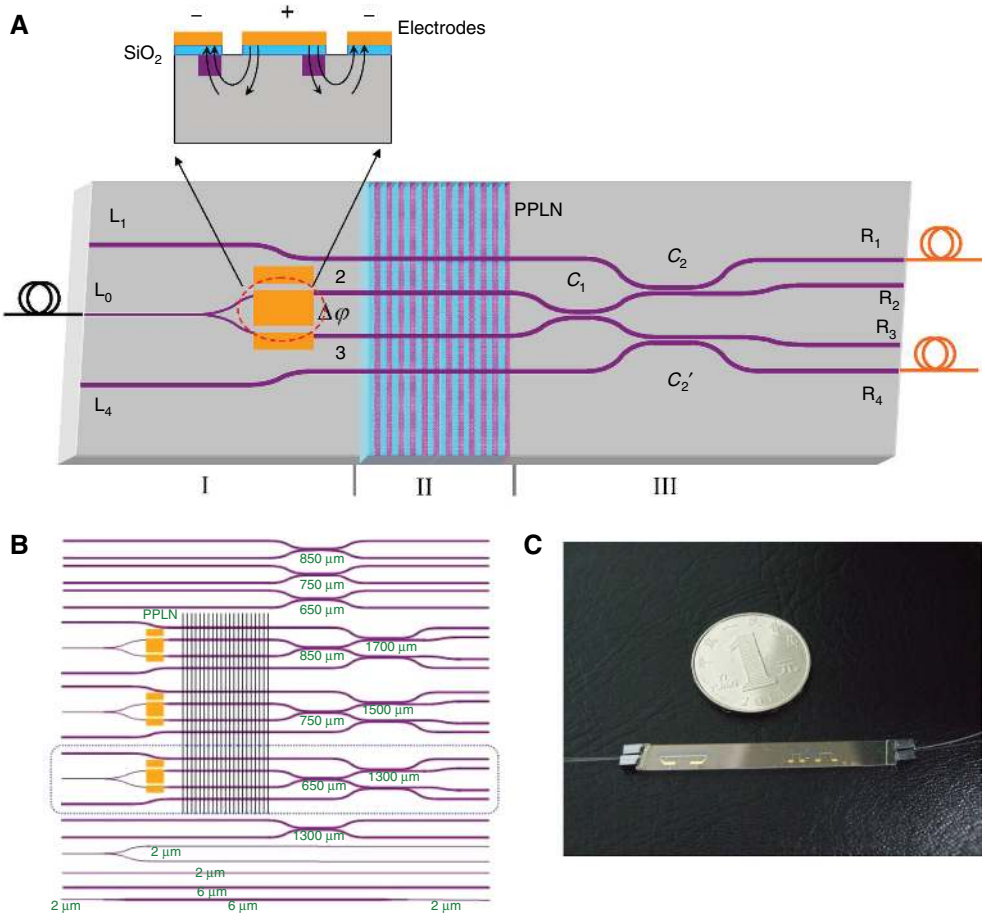

Figure 24: The photonic chip for generating and manipulating entangled photons.
(A) Schematic diagram of this chip. Top inset: cross-section view of the electro-optic modulator. (B) Overview of the chip. (C) Photograph of the chip. Reprinted figure with permission from Jin et al. [196]. Copyright (2019) by the American Physical Society.

Although these quantum memories are achieved in discrete LN components, the concept can be adopted to LNOI waveguides by doping LN thin film with erbium or thulium before bonding to the insulator layer. Another totally different physical mechanism to achieving quantum memory is based on an optical two-level system consisting of two coupled electro-optic microrings made from LNOI (Figure 25A) [75]. As shown in Figure 25B, in this system, light couples to a bright-mode microring from a waveguide and then couples to the other dark-mode microring when a microwave pulse is applied. As the microwave is switched off, light is stored in the dark-mode microring without any external coupling. After the desired storage time, the second microwave pulse readouts light from the dark to the bright-mode microring.

4.4 Metrology

In metrology, optical frequency combs have demonstrated many applications including ranging and spectroscopy with high performance [203, 204]. As mentioned in Section 3.3, Optical frequency comb, LNOI is the ideal material platform for achieving second-order nonlinear comb and electro-optic comb, opening the door of miniaturized metrology based on integrated LN frequency combs.

Optical frequency comb-based ranging system has the advantages of long measurement distance, high precision, and high-speed sampling [203]. Such a ranging system can be achieved based on an electro-optic frequency comb. As shown in Figure 26, we input the comb spectrum into an unbalanced MZI with one arm including the distance under test and the delay fiber. For different repetition rates, the unbalanced length corresponds to different numbers (either an integer or a decimal number) of light pulses. When unbalanced length corresponds to an integer number of pulses (N_p, N_p+1, N_p+2 …) at certain repetition rates (f_p, $f_p+\Delta f$, $f_p+2\Delta f$ …), the unbalanced length brings zero additional phase to arm #2. Thus, light in arm #1 and #2 can transmit out of the interferometer at the same phase and lead to constructive interferences. Such constructive interferences happen at a series of

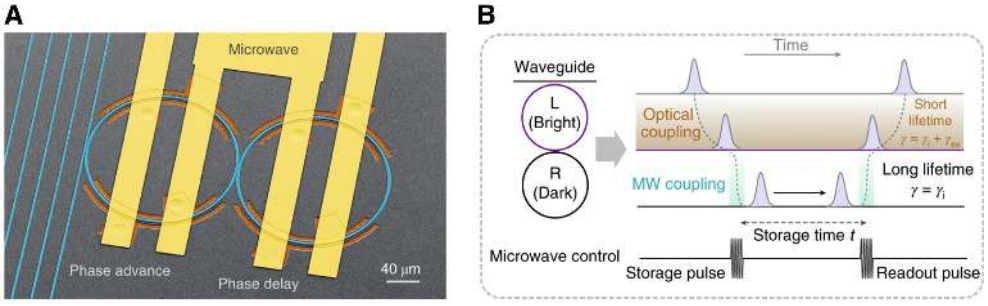

Figure 25: Electronically programmable photonic molecule.
(A) False-colored scanning electron microscope image of the coupled microring resonators, (B) operating principle of on-demand storage and retrieval of light based on a photonic dark mode. Reprinted by permission from Zhang et al. [75], Springer Nature Limited, copyright 2019.

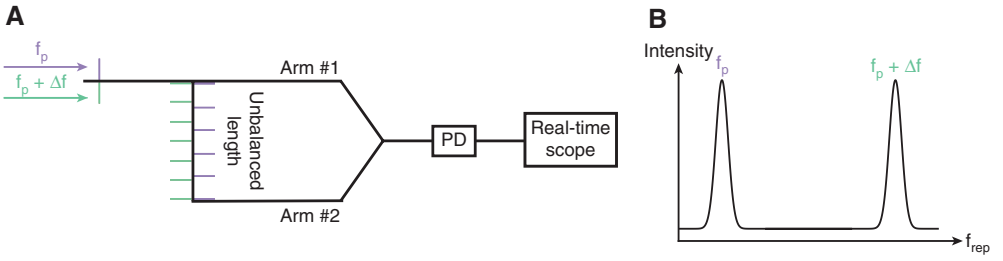

Figure 26: Principle of optical frequency comb-based ranging system.
(A) Two pulse trains come from a repetition rate adjustable optical frequency comb. Constructive temporal interference happens when the unbalanced length (including the distance under test and the length of delay fiber) corresponds to an integer number of pulses.
(B) So, by sweeping the repetition rate, constructive interference happens at different repetition rate according to the distance under test. Once the two peaks are found by changing the repetition rate, the distance is measured. A larger repetition-rate sweeping range leads to a larger range of measurable distance. A fast sweeping speed of repetition rate enables measuring the speed of a fast-moving object.
PD, photodiode. See Kayes and Rochette [205] and Yang et al. [206] for details.

peaks in the intensity spectrum as a function of repetition rate when we sweep the repetition rate (Figure 26B). These peaks correspond to repetition rates f_p, $f_p+\Delta f$, $f_p+2\Delta f$ …, which correspond to the number of pulses in the unbalanced length equaling to N_p, N_p+1, N_p+2 …. By measuring the spacing between two adjacent peaks (Δf), we can obtain the distance [205, 207]. For example, if the unbalanced length equals L, which corresponds to N_p pulses for repetition rate f_p, and corresponds to N_p+1 pulses for repetition rate $f_p+\Delta f$, we can get $L=N_p v_g/f_p$ and $L=(N_p+1)v_g/(f_p+\Delta f)$, where v_g is the group velocity of light traveling in the unbalanced length. Finally, we can obtain $L=v_g/\Delta f$ by measuring Δf (Figure 26).

Although this ranging system is based on an optical frequency comb source consisting of a single-mode Brillouin laser processed with phase modulation, pulse compression, and FWM [208], such a comb source can be simply replaced by an integrated LNOI waveguide–based comb [132] (Section 3.3, Optical frequency comb), simplifying the ranging system dramatically. And, the cavity-free LNOI waveguide–based comb can still provide an arbitrary repetition rate and a large repetition-rate variation range, which is only limited by the RF source. Furthermore, because integrated LNOI waveguide–based comb can sweep the repetition rate in a big range with an ultrafast speed, it could yield a compact ranging system with large measurement range and high distance acquisition rate, enabling the tracking of fast-moving objects in a huge range and its applications in autonomous vehicle and remote sensing.

Frequency comb spectroscopy has broad applications in molecular spectroscopy, environmental sensing, chemistry, biology, and medicine [204]. As one of the most promising spectrometric approaches with frequency combs, dual-comb spectroscopy uses a frequency comb to interrogate the sample and then beat with the other comb with slightly different repetition rate, producing a comb in RF domain, which can be measured by electronics [209]. As a result, dual-comb spectroscopy does not need moving parts, enabling rapid and precise measurements over a board spectrum. Additionally, dual-comb spectroscopy has the advantages of using laser beam instead of incoherent light source, absolute frequency calibration, and the negligible contribution of the instrumental line shape. Based on integrated LN electro-optic frequency combs [84], a dual-comb spectroscopy source can be achieved with a spectral resolution around 10 GHz (Figure 27A) [210]. Such a dual-comb spectroscopy features a programmable refresh rate by leveraging the tunable repetition rate of the electro-optic combs (Figure 27C).

5 Summary and outlook

Lithium niobate on insulator combined with ridge-waveguide fabrication technique enables various integrated

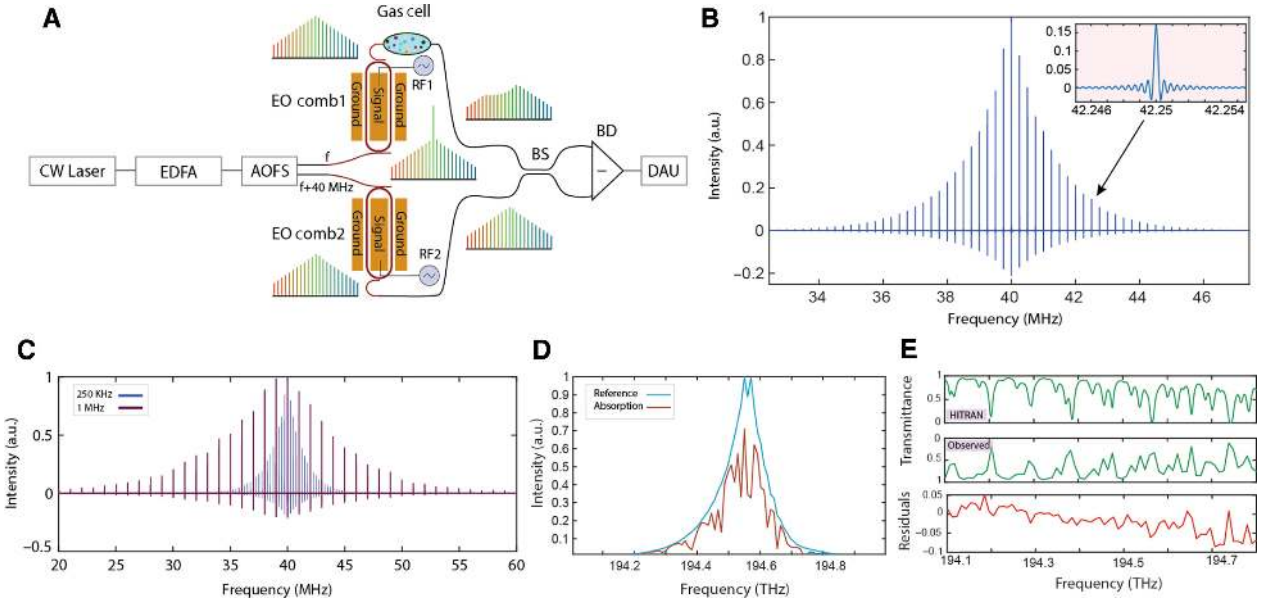

Figure 27: Dual-comb spectroscopy.
(A) Schematic of dual-comb spectroscopy with integrated LN electro-optic frequency combs. (B) Measured spectrum of dual comb (measurement time 195 s). (C) Transmission spectra of the dual comb with difference in microwave modulation frequencies equal 0.25 and 1 MHz, demonstrating the reconfigurable refresh rate. (D) Absorption spectra of acetylene. (E) Comparison of measured transmission spectrum with HITRAN database and the corresponding residuals. Copyright from [210].

optical structures including waveguide, resonator, and PPLN. These structures can fully leverage the extraordinary linear, nonlinear, and electro-optic properties of LN to achieve many integrated devices, such as electro-optic modulator and optical frequency comb, with record-high performance. These devices have the potential of revolutionizing LN's traditional application areas including optical communications, microwave photonics, and quantum optics, as well as opening the door of many new applications, such as metrology.

In addition to the applications we have reviewed, we also envision integrated LNOI devices' potential applications in high-performance nonlinear and quantum optics; devices in UV, visible, and mid-IR regimes; and optical computing and signal processing. Finally, we discuss the challenges and opportunities of LNOI devices from the viewpoints of design, fabrication, and system-on-a-chip followed by the potential solutions.

5.1 High-performance nonlinear and quantum optics

By combining the LN's high second-order nonlinearity and flexibility in achieving various on-chip structures, we could realize many integrated nonlinear optical devices such as wavelength converters in the form of mode multiplexer/demultiplexer. Furthermore, we can achieve many quantum-optics applications via nonlinear processes, such as generating entangled photon pair via SPDC. In addition to the quantum-optics applications oriented in nonlinear optics, LN has also been used to demonstrate heralded single-photon sources, quantum interfaces, and quantum memories [42, 202]. So far, most of these quantum-optics applications are based on titanium-diffused or proton-exchanged LN waveguides. Although those applications have already taken advantage of the optical properties of LN, we believe that LNOI and ridge structures will be able to boost the performance of integrated LN quantum photonics dramatically.

Lithium niobate on insulator is a competitive material platform for some third-order nonlinear processes, including Kerr frequency comb and Raman scattering, with many potential applications including optical communications, quantum optics, microwave photonics, and spectroscopy [211, 212]. So far, there are only very few studies of third-order nonlinear processes in LNOI [146]. Thus, studying third-order nonlinear properties of LNOI structures is highly demanded. For example, generating Kerr frequency comb or soliton mode locking needs to suppress SRS. So, it is imperative to study the SRS in LNOI-based structures and devices.

5.2 Devices in UV, visible, and mid-IR regimes

Lithium niobate has a wide transparency window ranging from UV to mid-IR. By using wavelength upconversion or downconversion based on nonlinear optical processes, we could generate mid-IR or visible light with pump light in telecom wavelengths. For example, Yue et al. [213] demonstrated DFG between a picosecond pulse fiber laser and a synchronized fiber laser, generating a high average power mid-IR picosecond pulse bunch output. Moreover, we could generate near-UV light based on Mg-doped LN. Those on-chip light sources combined with other on-chip LN structures enable various devices in UV, visible, and mid-IR regimes.

Optical sensing is a typical application of LNOI-based devices in mid-IR. Optical sensing is usually achieved by identifying different substances via probing their characteristic absorption peak. Many molecular substances show absorption peaks in the mid-IR regime, in which optical signals can be generated via DFG in LNOI-based devices, such as PPLNs. By combing LNOI-based mid-IR light sources and sensing structures, including waveguide gratings, tapered waveguides and microdisk/microring resonators (e.g. a high Q LNOI double disk [62]), we can realize mid-IR sensors on a single chip. Considering that integrated photonic sensors have broad applications in various areas including chemical and environmental sensing, LNOI-based photonic sensing is a promising direction for future development.

5.3 Optical computing and signal processing

At the era that Moore's law reaches its physical limitation, humans are actively searching for the next-generation computing mechanisms. As one of the promising candidates, optical computing has the potential advantages of higher computation speed, lower energy consumption, and better compatibility with optical communication system. Optical computing can be realized via self-configuring photonic networks [136, 214–216]. The basic component of such a network is an MZI as controllable reflector and phase shifter. By fully taking advantage of the nonlinear response on femtosecond timescales, low optical and microwave losses, and scalability of LNOI photonics, we may be able to achieve integrated self-configuring photonic networks with ultrahigh reconfiguration speed and low energy cost.

5.4 Challenges and opportunities

Despite LNOI-based devices' fast development in recent years and various potential applications, LNOI still meets challenges from design, fabrication, and system-on-a-chip. To overcome these challenges, we envision future development of LNOI from the following aspects:

(1) Inverse design of LNOI-based structures and devices. Most LNOI-based structures and devices in this review are designed according to the prior experience and knowledge, followed by optimization through parameter sweeps or random/combinatorial optimization algorithms, such as genetic algorithms. Such a design methodology restricts the parameter space to a few degrees of freedom (DOFs), preventing us from fully maximizing the FOM and achieving the best performance. In some complicated cases, such as designs with multiple FOMs, we may even be unable to achieve a suitable solution based solely on our existing knowledge, for example, designing an LNOI soliton frequency comb whose multimode coupling results in a desired broadband dispersion supporting solitons [171]. A potential solution is designing LNOI-based structures and devices inversely from desired characteristics to physical systems by using effective algorithms [217]. Inverse design can treat every single pixel in the design domain as a DOF, enabling the exploration of a much larger parameter space to fully maximize the FOMs. Distinct from conventional optimization techniques, many inverse-design algorithms, such as topology optimization, are guided by gradient information, enabling the convergence to an optimal structure within a few iterations.

(2) Mass production of LNOI-based devices at low cost and high fidelity. Most of the LNOI fabrication techniques we have reviewed so far are only suitable for prototyping nanostructures in academic laboratories. For example, direct etching ridge structures with a minimum feature size of a few hundred nanometers require patterning the resist by using EBL, limiting the fabrication speed drastically. For another example, direct laser writing needs to scan the laser beam spot over the entire sample volume, making fabrication of large-volume sample extremely time consuming [61, 218]. Two potential solutions to achieve mass production of LNOI-based devices are photolithography and nanoimprinting. By replacing EBL with photolithography, we shall be able to patterning the entire wafer in a single exposure [219]. On the other hand, nanoimprinting can efficiently transfer the pattern from mold to resist despite the time-consuming fabrication of the mold by using EBL [220].

(3) System on an LNOI chip. Despite the fast development of LNOI in integrated electro-optic and nonlinear devices, many other functional devices, including polarization controllers and converters, light sources, and detectors, as well as optical amplifiers, are still needed to achieve system on an LNOI chip. To compensate the fact that LN does not have direct bandgap, light sources and detectors may be integrated to LNOI via heterostructuring other materials such as III-V, InP, and Ge [221, 222]. Optical amplifiers in LNOI may be achieved by doping LNOI structures, such as waveguides and resonators, with gain media, such as erbium and thulium [223]. A big challenge may be the high temperature required by erbium diffusion due to the fact that LNOI wafers made by bounding are sensitive to high temperature [39, 65].

Acknowledgment: We would like to thank Prof. Cheng Wang for the helpful discussion.

References

[1] Arizmendi L. Photonic applications of lithium niobate crystals. Phys Status Solidi A 2004;201:253–83.
[2] Jalali B, Fathpour S. Silicon photonics. J Lightwave Technol 2006;24:4600–15.
[3] Lim AE-J, Junfeng S, Qing F, et al. Review of silicon photonics foundry efforts. IEEE J Sel Top Quant 2014;20:405–16.
[4] Levy JS, Gondarenko A, Foster MA, Turner-Foster AC, Gaeta AL, Lipson M. CMOS-compatible multiple-wavelength oscillator for on-chip optical interconnects. Nat Photonics 2009;4:37–40.
[5] Okawachi Y, Saha K, Levy JS, Wen YH, Lipson M, Gaeta AL. Octave-spanning frequency comb generation in a silicon nitride chip. Opt Lett 2011;36:3398–400.
[6] Ogiso Y, Ozaki J, Ueda Y, et al. Over 67 GHz bandwidth and 1.5 V Vπ InP-based optical IQ modulator with n-i-p-n heterostructure. J Lightwave Technol 2017;35:1450–5.
[7] Nikogosyan DN. Nonlinear optical crystals: a complete survey, 1st ed. New York, NY: Springer, 2005.
[8] Schmidt RV, Kaminow IP. Metal-diffused optical waveguides in $LiNbO_3$. Appl Phys Lett 1974;25:458–60.
[9] Neyer A, Sohler W. High-speed cutoff modulator using a Ti-diffused $LiNbO_3$ channel waveguide. Appl Phys Lett 1979;35:256–8.
[10] Wooten EL, Kissa KM, Yi-Yan A, et al. A review of lithium niobate modulators for fiber-optic communications systems. IEEE J Sel Top Quant 2000;6:69–82.
[11] Fukuma M, Noda J. Optical properties of titanium-diffused $LiNbO_3$ strip waveguides and their coupling-to-a-fiber characteristics. Appl Opt 1980;19:591–7.
[12] Jackel JL, Rice CE, Veselka JJ. Proton exchange for high-index waveguides in $LiNbO_3$. Appl Phys Lett 1982;41:607–8.
[13] Wong KK, La Rue RMD, Wright S. Electro-optic-waveguide frequency translator in $LiNbO_3$ fabricated by proton exchange. Opt Lett 1982;7:546–8.
[14] Suchoski PG, Findakly TK, Leonberger FJ. Stable low-loss proton-exchanged $LiNbO_3$ waveguide devices with no electro-optic degradation. Opt Lett 1988;13:1050–2.

[15] Vohra ST, Mickelson AR, Asher SE. Diffusion characteristics and waveguiding properties of proton-exchanged and annealed $LiNbO_3$ channel waveguides. J Appl Phys 1989;66:5161–74.
[16] Stepanenko O, Quillier E, Tronche H, Baldi P, De Micheli M. Highly confining proton exchanged waveguides on Z-cut $LiNbO_3$ with preserved nonlinear coefficient. IEEE Photonic Tech L 2014;26:1557–60.
[17] Yi-Yan A. Index instabilities in proton-exchanged $LiNbO_3$ waveguides. Appl Phys Lett 1983;42:633–5.
[18] Korkishko YN, Fedorov VA, De Micheli M, Baldi P, Hadi KE, Leycuras A. Relationships between structural and optical properties of proton-exchanged waveguides on Z-cut lithium niobate. Appl Opt 1996;35:7056–60.
[19] Cai L, Kang Y, Hu H. Electric-optical property of the proton exchanged phase modulator in single-crystal lithium niobate thin film. Opt Express 2016;24:4640–7.
[20] Levy M, Osgood RM, Liu R, et al. Fabrication of single-crystal lithium niobate films by crystal ion slicing. Appl Phys Lett 1998;73:2293–5.
[21] Poberaj G, Hu H, Sohler W, Günter P. Lithium niobate on insulator (LNOI) for micro-photonic devices. Laser Photonics Rev 2012;6:488–503.
[22] Poberaj G, Koechlin M, Sulser F, Guarino A, Hajfler J, Günter P. Ion-sliced lithium niobate thin films for active photonic devices. Opt Mater 2009;31:1054–8.
[23] Rabiei P, Gunter P. Optical and electro-optical properties of submicrometer lithium niobate slab waveguides prepared by crystal ion slicing and wafer bonding. Appl Phys Lett 2004;85:4603–5.
[24] Jinan Jingzheng Electronics Co., Ltd. https://www.nanoln.com/.
[25] Guarino A, Poberaj G, Rezzonico D, Degl'Innocenti R, Günter P. Electro-optically tunable microring resonators in lithium niobate. Nat Photonics 2007;1:407–10.
[26] Chen L and Reano RM. Compact electric field sensors based on indirect bonding of lithium niobate to silicon microrings. Opt Express 2012;20:4032–8.
[27] Rabiei P, Ma J, Khan S, Chiles J, Fathpour S. Heterogeneous lithium niobate photonics on silicon substrates. Opt Express 2013;21:25573–81.
[28] Chen L, Wood MG, Reano RM. 12.5 pm/v hybrid silicon and lithium niobate optical microring resonator with integrated electrodes. Opt Express 2013;21:27003–10.
[29] Cao L, Aboketaf A, Wang Z, Preble S. Hybrid amorphous silicon (a-si:h)–$LiNbO_3$ electro-optic modulator. Opt Commun 2014;330:40–4.
[30] Cai L, Kong R, Wang Y, Hu H. Channel waveguides and y-junctions in X-cut single-crystal lithium niobate thin film. Opt Express 2015;23:29211–21.
[31] Cai L, Wang Y, Hu H. Low-loss waveguides in a single-crystal lithium niobate thin film. Opt Lett 2015;40:3013–6.
[32] Chen L, Chen J, Nagy J, Reano RM. Highly linear ring modulator from hybrid silicon and lithium niobate. Opt Express 2015;23:13255–64.
[33] Rao A, Patil A, Chiles J, Malinowski M, Novak S, Richardson K, Rabiei P, Fathpour S. Heterogeneous microring and Mach–Zehnder modulators based on lithium niobate and chalcogenide glasses on silicon. Opt Express 2015;23:22746–52.
[34] Bo F, Wang J, Cui J, et al. Lithium–niobate–silica hybrid whispering-gallery-mode resonators. Adv Mater 2015;27:8075–81.
[35] Jin S, Xu L, Zhang H, Li Y. $LiNbO_3$ thin-film modulators using silicon nitride surface ridge waveguides. IEEE Photonic Tech L 2016;28:736–9.
[36] Chang L, Pfeiffer MH, Volet N, et al. Heterogeneous integration of lithium niobate and silicon nitride waveguides for wafer-scale photonic integrated circuits on silicon. Opt Lett 2017;42:803–6.
[37] Witmer JD, Valery JA, Arrangoiz-Arriola P, Sarabalis CJ, Hill JT, Safavi-Naeini AH. High-Q photonic resonators and electro-optic coupling using silicon-on-lithium–niobate. Sci Rep 2017;7:46313.
[38] Bazzan M, Sada C. Optical waveguides in lithium niobate: recent developments and applications. Appl Phys Rev 2015;2:040603.
[39] Rao A, Fathpour S. Compact lithium niobate electrooptic modulators. IEEE J Sel Top Quant 2018;24:1–14.
[40] Rao A, Patil A, Rabiei P, et al. High-performance and linear thin-film lithium niobate Mach–Zehnder modulators on silicon up to 50 GHz. Opt Lett 2016;41:5700–3.
[41] Liang H, Luo R, He Y, Jiang H, Lin Q. High-quality lithium niobate photonic crystal nanocavities. Optica 2017;4:1251–8.
[42] Boes A, Corcoran B, Chang L, Bowers J, Mitchell A. Status and potential of lithium niobate on insulator (LNOI) for photonic integrated circuits. Laser Photonics Rev 2018;12:1700256.
[43] Honardoost A, Safian R, Rao A, Fathpour S. High-speed modeling of ultracompact electrooptic modulators. J Lightwave Technol 2018;36:5893–902.
[44] Hu H, Ricken R, Sohler W, Wehrspohn RB. Lithium niobate ridge waveguides fabricated by wet etching. IEEE Photonic Tech L 2007;19:417–9.
[45] Ulliac G, Calero V, Ndao A, Baida FI, Bernal MP. Argon plasma inductively coupled plasma reactive ion etching study for smooth sidewall thin film lithium niobate waveguide application. Opt Mater 2016;53:1–5.
[46] Escale MR, Pohl D, Sergeyev A, Grange R. Extreme electro-optic tuning of Bragg mirrors integrated in lithium niobate nanowaveguides. Opt Lett 2018;43:1515–8.
[47] Lacour F, Courjal N, Bernal MP, Sabac A, Bainier C, Spajer M. Nanostructuring lithium niobate substrates by focused ion beam milling. Opt Mater 2005;27:1421–5.
[48] Ulliac G, Guichardaz B, Rauch J-Y, Queste S, Benchabane S, Courjal N. Ultra-smooth $LiNbO_3$ micro and nano structures for photonic applications. Microelectron Eng 2011;88:2417–9.
[49] Krasnokutska I, Tambasco JJ, Li X, Peruzzo A. Ultra-low loss photonic circuits in lithium niobate on insulator. Opt Express 2018;26:897–904.
[50] Wang C, Zhang M, Chen X, et al. Integrated lithium niobate electro-optic modulators operating at CMOS-compatible voltages. Nature 2018;562:101–4.
[51] Wang J, Bo F, Wan S, et al. High-Q lithium niobate microdisk resonators on a chip for efficient electro-optic modulation. Opt Express 2015;23:23072–8.
[52] Gondarenko A, Levy JS, Lipson M. High confinement micron-scale silicon nitride high Q ring resonator. Opt Express 2009;17:11366–70.
[53] Hu H, Ricken R, Sohler W. Lithium niobate photonic wires. Opt Express 2009;17:24261–8.
[54] Wang C, Xiong X, Andrade N, et al. Second harmonic generation in nano-structured thin-film lithium niobate waveguides. Opt Express 2017;25:6963–73.
[55] Wang C, Zhang M, Stern B, Lipson M, Loncar M. Nanophotonic lithium niobate electro-optic modulators. Opt Express 2018;26:1547–55.

[56] Nagata H, Mitsugi N, Shima K, Tamai M, Haga EM. Growth of crystalline LiF on CF4 plasma etched $LiNbO_3$ substrates. J Cryst Growth 1998;187:573–6.
[57] Wu R, Wang M, Xu J, et al. Long low-loss-lithium niobate on insulator waveguides with sub-nanometer surface roughness. Nanomaterials (Basel) 2018;8:910.
[58] Wu R, Zhang J, Yao N, et al. Lithium niobate micro-disk resonators of quality factors above 10(7). Opt Lett 2018;43:4116–9.
[59] Wang M, Wu R, Lin J, et al. Chemo-mechanical polish lithography: a pathway to low loss large-scale photonic integration on lithium niobate on insulator. Quant Eng 2019;1:e9.
[60] Volk MF, Suntsov S, Ruter CE, Kip D. Low loss ridge waveguides in lithium niobate thin films by optical grade diamond blade dicing. Opt Express 2016;24:1386–91.
[61] Wang M, Xu Y, Fang ZY, et al. On-chip electro-optic tuning of a lithium niobate microresonator with integrated in-plane microelectrodes. Opt Express 2017;25:124–9.
[62] Fang Z, Yao N, Wang M, et al. Fabrication of high quality factor lithium niobate double-disk using a femtosecond laser. Int J Optomechatronics 2017;11:47–54.
[63] Ahmed ANR, Shi S, Zablocki M, Yao P, Prather DW. Tunable hybrid silicon nitride and thin-film lithium niobate electro-optic microresonator. Opt Lett 2019;44:618–21.
[64] Chang L, Li Y, Volet N, Wang L, Peters J, Bowers JE. Thin film wavelength converters for photonic integrated circuits. Optica 2016;3:531–5.
[65] Li S, Cai L, Wang Y, Jiang Y, Hu H. Waveguides consisting of single-crystal lithium niobate thin film and oxidized titanium stripe. Opt Express 2015;23:24212–9.
[66] Hunsperger RG. Integrated optics: theory and technology. Cham, Switzerland, Springer, 2009.
[67] He M, Xu M, Ren Y, et al. High-performance hybrid silicon and lithium niobate Mach–Zehnder modulators for 100 Gbit s^{-1} and beyond. Nat Photonics 2019;13:359–64.
[68] Reed GT, Mashanovich GZ, Gardes FY, et al. Recent breakthroughs in carrier depletion based silicon optical modulators. Nanophotonics 2014;3:229–45.
[69] Zhang M, Wang C, Cheng R, Shams-Ansari A, Loncar M. Monolithic ultra-high-Q lithium niobate microring resonator. Optica 2017;4.
[70] Muttalib MFA, Chen R, Pearce S, Charlton M. Tapered nanowire waveguide layout for rapid optical loss measurements by cut back technique. In: Konstantin LV, editors. Nonlinear Frequency Generation and Conversion: Materials, Devices, and Applications XII. Bellingham, WA, USA, SPIE, 2013;8604:133–140.
[71] Regener R, Sohler W. Loss in low-finesse Ti:$LiNbO_3$ optical waveguide resonators. Appl Phys B 1985;36:143–7.
[72] Saleh BE, Teich MC. Fundamentals of photonics. New York, USA, John Wiley & Sons, 2019.
[73] Lin J, Yao N, Hao Z, et al. Broadband quasi-phase-matched harmonic generation in an on-chip monocrystalline lithium niobate microdisk resonator. Phys Rev Lett 2019;122:173903.
[74] Yu M, Desiatov B, Okawachi Y, Gaeta AL, Loncar M. Coherent two-octave-spanning supercontinuum generation in lithium–niobate waveguides. Opt Lett 2019;44:1222–5.
[75] Zhang M, Wang C, Hu Y, et al. Electronically programmable photonic molecule. Nat Photonics 2019;13:36–40.
[76] Foreman MR, Swaim JD, Vollmer F. Whispering gallery mode sensors. Adv Opt Photonics 2015;7:168–240.
[77] Shi L, Zhu T, Huang D, Liu M, Deng M, Huang W. In-fiber whispering-gallery-mode resonator fabricated by femtosecond laser micromachining. Opt Lett 2015;40:3770–3.
[78] Wang C, Burek MJ, Lin Z, et al. Integrated high quality factor lithium niobate microdisk resonators. Opt Express 2014;22:30924–33.
[79] Zhang J, Fang Z, Lin J, et al. Fabrication of crystalline microresonators of high quality factors with a controllable wedge angle on lithium niobate on insulator. Nanomaterials 2019;9:1218-1-7.
[80] Liu S, Zheng Y, Fang Z, Ye X, Cheng Y, Chen X. Effective four-wave mixing in the lithium niobate on insulator microdisk by cascading quadratic processes. Opt Lett 2019;44:1456–9.
[81] Ge L, Jiang H, Liu Y, et al. Quality improvement and mode evolution of high-Q lithium niobate micro-disk induced by "light annealing". Opt Mater Express 2019;9:1632–9.
[82] Cai M, Painter O, Vahala KJ. Observation of critical coupling in a fiber taper to a silica-microsphere whispering-gallery mode system. Phys Rev Lett 2000;85:74–7.
[83] Bahadori M, Yang Y, Goddard LL, Gong S. High performance fully etched isotropic microring resonators in thin-film lithium niobate on insulator platform. Opt Express 2019;27:22025–39.
[84] Zhang M, Buscaino B, Wang C, et al. Broadband electro-optic frequency comb generation in a lithium niobate microring resonator. Nature 2019;568:373–7.
[85] Tervonen A, Honkanen S, Najafi SIJOE. Analysis of symmetric directional couplers and asymmetric Mach–Zehnder interferometers as 1.30- and 1.55-micron dual-wavelength demultiplexers. Opt Eng 1993;32:2083–91.
[86] He Y, Liang H, Luo R, Li M, Lin Q. Dispersion engineered high quality lithium niobate microring resonators. Opt Express 2018;26:16315–22.
[87] Joannopoulos JD. Photonic Crystals: Molding the Flow of light. Princeton, NJ: Princeton University Press, 1995.
[88] Quan Q, Deotare PB, Loncar M. Photonic crystal nanobeam cavity strongly coupled to the feeding waveguide. Appl Phys Lett 2010;96:203102.
[89] Li M, Liang H, Luo R, He Y, Ling J, Lin Q. Photon-level tuning of photonic nanocavities. Optica 2019;6:860–3.
[90] Jiang H, Liang H, Luo R, Chen X, Chen Y, Lin Q. Nonlinear frequency conversion in one dimensional lithium niobate photonic crystal nanocavities. Appl Phys Lett 2018;113:021104.
[91] Wang R, Bhave SA. Free-standing high quality factor thin-film lithium niobate micro-photonic disk resonators. Optics 2014, arXiv:1409.6351v1.
[92] Wang C, Zhang M, Yu M, Zhu R, Hu H, Loncar M. Monolithic lithium niobate photonic circuits for Kerr frequency comb generation and modulation. Nat Commun 2019;10:978.
[93] Fang Z, Haque S, Lin J, et al. Real-time electrical tuning of an optical spring on a monolithically integrated ultrahigh Q lithium nibote microresonator. Opt Lett 2019;44:1214–7.
[94] Zheng Y, Fang Z, Liu S, Cheng Y, Chen X. High-Q exterior whispering-gallery modes in a double-layer crystalline microdisk resonator. Phys Rev Lett 2019;122:253902.
[95] Chen B, Xu C, Zhou B, Nihei Y, Harada A. All-optical variable-in variable-out wavelength conversions by using MgO:$LiNbO_3$ quasiphase matched wavelength converters. Jpn J Appl Phys 2001;40:1370–2.
[96] Parameswaran KR, Route RK, Kurz JR, Roussev RV, Fejer MM, Fujimura M. Highly efficient second-harmonic generation in buried waveguides formed by annealed and reverse proton exchange in periodically poled lithium niobate. Opt Lett 2002;27:179–81.

[97] Genereux F, Baldenberger G, Bourliaguet B, Vallee R. Low-voltage tunable second-harmonic generation in an X-cut periodically poled lithium niobate waveguide. Opt Lett 2007;32:1108–10.
[98] Gui L, Hu H, Garciagranda M, Sohler W. Local periodic poling of ridges and ridge waveguides on X- and Y-cut $LiNbO_3$ and its application for second harmonic generation. Opt Express 2009;17:3923–8.
[99] Tang CL, Bey P. Phase matching in second-harmonic generation using artificial periodic structures. IEEE J Quantum Elect 1973;9:9–17.
[100] Yamada M, Nada N, Saitoh M, Watanabe K. First-order quasi-phase matched $LiNbO_3$ waveguide periodically poled by applying an external field for efficient blue second-harmonic generation. Appl Phys Lett 1993;62:435–6.
[101] Myers LE, Eckardt RC, Fejer MM, Byer RL, Bosenberg WR, Pierce JW. Quasi-phase-matched optical parametric oscillators in bulk periodically poled $LiNbO_3$. J Opt Soc Am B Opt Phys 1995;12:2102–16.
[102] Langrock C, Kumar S, McGeehan JE, Willner AE, Fejer MM. All-optical signal processing using χ^2 nonlinearities in guided-wave devices. J Lightwave Technol 2006;24: 2579–92.
[103] Bouwmeester D, Pan J, Mattle K, Eibl M, Weinfurter H, Zeilinger A. Experimental quantum teleportation. Nature 1997;390:575–9.
[104] Phillips CR, Langrock C, Pelc JS, Fejer MM, Hartl I, Fermann ME. Supercontinuum generation in quasi-phasematched waveguides. Opt Express 2011;19:18754–73.
[105] Roussev RV, Langrock C, Kurz JR, Fejer MM. Periodically poled lithium niobate waveguide sum-frequency generator for efficient single-photon detection at communication wavelengths. Opt Lett 2004;29:1518–20.
[106] Nagy JT and Reano RM. Reducing leakage current during periodic poling of ion-sliced X-cut MgO doped lithium niobate thin films. Opt Mater Express 2019;9:3146–55.
[107] Wang C, Langrock C, Marandi A, et al. Ultrahigh-efficiency wavelength conversion in nanophotonic periodically poled lithium niobate waveguides. Optica 2018;5:1438–41.
[108] Wolf R, Jia Y, Bonaus S, et al. Quasi-phase-matched nonlinear optical frequency conversion in on-chip whispering galleries. Optica 2018;5:872–5.
[109] Lu J, Surya JB, Liu X, et al. Periodically poled thin film lithium niobate microring resonators with a second-harmonic generation efficiency of 250,000%/W. 2019, arXiv:1911.00083.
[110] Gainutdinov RV, Volk TR, Zhang HH. Domain formation and polarization reversal under atomic force microscopy-tip voltages in ion-sliced $LiNbO_3$ films on $SiO_2/LiNbO_3$ substrates. Appl Phys Lett 2015;107.
[111] Mackwitz P, Rüsing M, Berth G, Widhalm A, Müller K, Zrenner A. Periodic domain inversion in X-cut single-crystal lithium niobate thin film. Appl Phys Lett 2016;108:152902-1-4.
[112] Taillaert D, Van Laere F, Ayre M, et al. Grating couplers for coupling between optical fibers and nanophotonic waveguides. Jpn J Appl Phys 2006;45A:6071–7.
[113] Chen X, Li C, Fung CKY, Lo SMG, Tsang HK. Apodized waveguide grating couplers for efficient coupling to optical fibers. IEEE Photonic Tech L 2010;22:1156–8.
[114] Kar A, Bahadori M, Gong S, Goddard LL. Realization of alignment-tolerant grating couplers for Z-cut thin-film lithium niobate. Opt Express 2019;27:15856–67.
[115] Taillaert D, Bogaerts W, Bienstman P, et al. An out-of-plane grating coupler for efficient butt-coupling between compact planar waveguides and single-mode fibers. IEEE J Quantum Elect 2002;38:949–55.
[116] Kato S, Chonan S, Aoki T. Micro-lensed single-mode optical fiber with high numerical aperture. Optics 2013, arXiv:1305.5937v1.
[117] Papes M, Cheben P, Benedikovic D, et al. Fiber-chip edge coupler with large mode size for silicon photonic wire waveguides. Opt Express 2016;24:5026–38.
[118] Pu M, Liu L, Ou H, Yvind K, Hvam JM. Ultra-low-loss inverted taper coupler for silicon-on-insulator ridge waveguide. Opt Commun 2010;283:3678–82.
[119] Kopp C, Bernabé S, Bakir BB, et al. Silicon photonic circuits: on-CMOS integration, fiber optical coupling, and packaging. IEEE J Sel Top Quant 2011;17:498–509.
[120] Mahmoud M, Cai L, Bottenfield C, Piazza G. Lithium niobate electro-optic racetrack modulator etched in Y-cut LNOI platform. IEEE Photonics J 2018;10:1–10.
[121] Jian J, Xu P, Chen H, et al. High-efficiency hybrid amorphous silicon grating couplers for sub-micron–sized lithium niobate waveguides. Opt Express 2018;26:29651–8.
[122] Siew SY, Saha SS, Tsang M, Danner AJ. Rib microring resonators in lithium niobate on insulator. IEEE Photonic Tech L 2016;28:573–6.
[123] Li G, Chen Y, Jiang H, Chen X. Broadband sum-frequency generation using d_{33} in periodically poled $LiNbO_3$ thin film in the telecommunications band. Opt Lett 2017;42:939–42.
[124] Wang C, Li Z, Kim MH, et al. Metasurface-assisted phase-matching-free second harmonic generation in lithium niobate waveguides. Nat Commun 2017;8:2098.
[125] He L, Zhang M, Shamsansari A, Zhu R, Wang C, Marko L. Low-loss fiber-to-chip interface for lithium niobate photonic integrated circuits. Opt Lett 2019;44:2314–7.
[126] Krasnokutska I, Tambasco JJ, Peruzzo A. Nanostructuring of LNOI for efficient edge coupling. Opt Express 2019;27: 16578–85.
[127] Tu X, Liow TY, Song J, Luo X, Fang Q, Yu M, Lo GQ. 50-Gb/s silicon optical modulator with traveling-wave electrodes. Opt Express 2013;21:12776–82.
[128] Baehr-Jones T, Ding R, Liu Y, et al. Ultralow drive voltage silicon traveling-wave modulator. Opt Express 2012;20: 12014–20.
[129] Kubota K, Noda J, Mikami O. Traveling wave optical modulator using a directional coupler $LiNbO_3$ waveguide. IEEE J Quantum Elect 1980;16:754–60.
[130] Kawanishi T, Sakamoto T, Izutsu M. High-speed control of lightwave amplitude, phase, and frequency by use of electrooptic effect. IEEE J Sel Top Quant 2007;13:79–91.
[131] Izutsu M, Yamane Y, Sueta T. Broad-band traveling-wave modulator using a $LiNbO_3$ optical waveguide. IEEE J Quantum Elect 1977;13:287–90.
[132] Ren T, Zhang M, Wang C, et al. An integrated low-voltage broadband lithium niobate phase modulator. IEEE Photonic Tech L 2019;31:889–92.
[133] Janner D, Tulli D, García-Granda M, Belmonte M, Pruneri V. Micro-structured integrated electro-optic $LiNbO_3$ modulators. Laser Photonics Rev 2009;3:301–13.
[134] Bridges WB, Sheehy FT, Schaffner JH. Velocity-matched electro-optic modulator. In: High-frequency analog fiber optic systems. Vol. 1371. International Society for Optics and Photonics, 1991:68–77.
[135] Pozar DM. Microwave engineering. New York, USA, John Wiley & Sons, 2009.

[136] Miller DAB. Perfect optics with imperfect components. Optica 2015;2:747–50.
[137] Jin M, Chen JY, Sua YM, Huang YP. High-extinction electro-optic modulation on lithium niobate thin film. Opt Lett 2019;44:1265–8.
[138] Ibarra Fuste JA, Santos Blanco MC. Bandwidth-length trade-off figures of merit for electro-optic traveling wave modulators. Opt Lett 2013;38:1548–50.
[139] Wang T, Chu C, Lin C. Electro-optically tunable microring resonators on lithium niobate. Opt Lett 2007;32:2777–9.
[140] Chen L, Xu Q, Wood MG, Reano RM. Hybrid silicon and lithium niobate electro-optical ring modulator. Optica 2014;1.
[141] Lee YS, Kim G, Kim W, Lee S, Lee W, Steier WH. Hybrid si-$LiNbO_3$ microring electro-optically tunable resonators for active photonic devices. Opt Lett 2011;36:1119–21.
[142] Zhou Z, Zhang S. Electro-optically tunable racetrack dual microring resonator with a high quality factor based on a lithium niobate-on-insulator. Opt Commun 2020;458:124718.
[143] Zhou G, Zhou L, Guo Y, et al. High-speed silicon electro-optic modulator based on a single multimode waveguide. In: Optical Fiber Communication Conference (OFC). Washington, DC, USA, Optical Society of America, 2019:W2A.10.
[144] Wang MR, Xu G, Lin F, Jannson T. Single-mode/multimode waveguide electro-optic grating coupler modulator. Appl Phys Lett 1995;66:2628–30.
[145] Boyd RW. Nonlinear optics, 3rd ed. Salt lake city, Utah, USA, Academic Press, 2008.
[146] Yu M, Okawachi Y, Cheng R, et al. Raman lasing and soliton mode-locking in lithium niobate microresonators. Light Sci Appl 2020;9:1–7.
[147] Wang C, Burek MJ, Lin Z, et al. Integrated lithium niobate nonlinear optical devices. CLEO. At San Jose, Washington, DC, USA, Optical Society of America. 2015:FW1D.1.
[148] Rodriguez AW, Soljacic M, Joannopoulos JD, Johnson SG. χ^2 and χ^3 harmonic generation at a critical power in inhomogeneous doubly resonant cavities. Opt Express 2007;15:w7303–18.
[149] Furst JU, Strekalov DV, Elser D, et al. Naturally phase-matched second-harmonic generation in a whispering-gallery-mode resonator. Phys Rev Lett 2010;104:153901.
[150] Luo R, Jiang H, Rogers S, Liang H, He Y, Lin Q. On-chip second-harmonic generation and broadband parametric down-conversion in a lithium niobate microresonator. Opt. Express 2017;25:24531–9.
[151] Kuo PS, Bravo-Abad J, Solomon GS. Second-harmonic generation using 4-quasi-phasematching in a GaAs whispering-gallery-mode microcavity. Nat Commun 2014;5:3109.
[152] Levy JS, Foster MA, Gaeta AL, Lipson M. Harmonic generation in silicon nitride ring resonators. Opt Express 2011;19:11415–21.
[153] Xiong C, Pernice WHP, Ryu KK, et al. Integrated GaN photonic circuits on silicon (100) for second harmonic generation. Opt Express 2011;19:10462–70.
[154] Mizuuchi K, Yamamoto K, Kato M. Harmonic blue light generation in bulk periodically poled MgO:$LiNbO_3$. Electron Lett 1996;32:2091–2.
[155] Jankowski M, Langrock C, Desiatov B, et al. Ultrabroadband nonlinear optics in nanophotonic periodically poled lithium niobate waveguides. Optica 2020;7:40–6.
[156] Luo R, He Y, Liang H, Li M, Lin Q. Highly tunable efficient second-harmonic generation in a lithium niobate nanophotonic waveguide. Optica 2018;5:1006–11.
[157] Moore J, Tomes M, Carmon T, Jarrahi M. Continuous-wave cascaded-harmonic generation and multi-photon Raman lasing in lithium niobate whispering-gallery resonators. Appl Phys Lett 2011;99:221111.
[158] Ye X, Liu S, Chen Y, Zheng Y, Chen X. Sum-frequency generation in lithium–niobate-on-insulator microdisk via modal phase matching. Opt Lett 2020;45:523–6.
[159] Sasagawa K, Tsuchiya M. Highly efficient third harmonic generation in a periodically poled MgO:$LiNbO_3$ disk resonator. Appl Phys Express 2009;2:122401.
[160] Liu S, Zheng Y, Chen X. Cascading second-order nonlinear processes in a lithium niobate-on-insulator microdisk. Opt Lett 2017;42:3626–9.
[161] Wang D, Ding T, Zheng Y, Chen X. Cascaded sum-frequency generation and electro-optic polarization coupling in the ppLNOI ridge waveguide. Opt Express 2019;27:15283–8.
[162] Chi J, Liu H, Huang N, Wang Z. High-performance mid-infrared frequency upconversion in lithium niobate waveguide patterned with metasurfaces. J Phys D Appl Phys 2019;52:035101-1-6.
[163] Leidinger M, Sturman B, Buse K, Breunig I. Strong forward-backward asymmetry of stimulated Raman scattering in lithium–niobate-based whispering gallery resonators. Opt Lett 2016;41:2823–6.
[164] Eckstein JN, Ferguson AI, Hänsch TW. High-resolution two-photon spectroscopy with picosecond light pulses. Phys Rev Lett 1978;40:847–50.
[165] Kippenberg TJ, Holzwarth R, Diddams SA. Microresonator-based optical frequency combs. Science 2011;332:555–9.
[166] Del'Haye P, Schliesser A, Arcizet O, Wilken T, Holzwarth R, Kippenberg TJ. Optical frequency comb generation from a monolithic microresonator. Nature 2007;450:1214–7.
[167] Wu Z, Ming Y, Xu F, Lu Y. Optical frequency comb generation through quasi-phase matched quadratic frequency conversion in a micro-ring resonator. Opt Express 2012;20:17192–200.
[168] Ho K, Kahn JM. Optical frequency comb generator using phase modulation in amplified circulating loop. IEEE Photonic Tech L 1993;5:721–5.
[169] Rueda A, Sedlmeir F, Kumari M, Leuchs G, Schwefel HGL. Resonant electro-optic frequency comb. Nature 2019;568:378–81.
[170] Kippenberg TJ, Spillane SM, Vahala KJ. Kerr-nonlinearity optical parametric oscillation in an ultrahigh-Q toroid microcavity. Phys Rev Lett 2004;93:083904.
[171] Kippenberg TJ, Gaeta AL, Lipson M, Gorodetsky ML. Dissipative Kerr solitons in optical microresonators. Science 2018;361:eaan8083.
[172] Kippenberg T, Spillane S, Vahala K. Kerr-nonlinearity optical parametric oscillation in an ultrahigh-Q toroid microcavity. Phys Rev Lett 2004;93:083904.
[173] Metcalf AJ, Fredrick C, Terrien RC, Papp SB, Diddams SA. 30 GHz electro-optic frequency comb spanning 300 THz in the near infrared and visible. Opt Lett 2019;44:2673–6.
[174] Yan M, Luo P, Iwakuni K, Millot G, Hansch TW, Picque N. Mid-infrared dual-comb spectroscopy with electro-optic modulators. Light Sci Appl 2017;6:e17076-1-6.
[175] Imany P, Odele OD, Jaramillovillegas JA, Leaird DE, Weiner AM. Characterization of coherent quantum frequency combs using electro-optic phase modulation. Phys Rev A 2018;97:013813-1-5.
[176] Rusing M, Weigel PO, Zhao J, Mookherjea S. Toward 3d integrated photonics including lithium niobate thin films: a bridge between electronics, radio frequency, and optical technology. IEEE Nanotechnol Mag 2019;13:18–33.

[177] Yariv A. Optical electronics in modern communications 1. Oxford, UK, Oxford University Press, 1997.
[178] Miller DA. Device requirements for optical interconnects to silicon chips. Proc IEEE 2009;97:1166–85.
[179] Mizuochi T, Miyata Y, Kobayashi T, et al. Forward error correction based on block turbo code with 3-bit soft decision for 10-Gb/s optical communication systems. IEEE J Sel Top Quant 2004;10:376–86.
[180] Xu Q, Schmidt BS, Pradhan S, Lipson M. Micrometre-scale silicon electro-optic modulator. Nature 2005;435:325–7.
[181] Koeber S, Palmer R, Lauermann M, et al. Femtojoule electro-optic modulation using a silicon-organic hybrid device. Light Sci Appl 2015;4:255.
[182] Lee M, Katz HE, Erben CG, et al. Broadband modulation of light by using an electro-optic polymer. Science 2002;298:1401–3.
[183] Aoki M, Suzuki M, Sano H, et al. InGaAs/inGaAsp MQW electroabsorption modulator integrated with a DFB laser fabricated by band-gap energy control selective area mocvd. IEEE J Quantum Elect 1993;29:2088–96.
[184] Sun C, Wade MT, Lee Y, et al. Single-chip microprocessor that communicates directly using light. Nature 2015;528:534–8.
[185] Haffner C, Chelladurai D, Fedoryshyn Y, et al. Low-loss plasmon-assisted electro-optic modulator. Nature 2018;556:483–6.
[186] Song X, Li R, Mi G, Suo J, Zhang Z, Li Y. Optoelectronic integrated circuits for growing datacenters: challenge, strategy, and evolution. SPIE OPTO 2019, doi 10.1117/12.2507919.
[187] G. L. M. Group. 400g-fr4 technical specification. http://www.100glambda.com/specifications/send/2-specifications/7-400g-fr4-technical-spec-d2p0-2. 2018.
[188] Marpaung D, Yao J, Capmany J. Integrated microwave photonics. Nat Photonics 2019;13:80–90.
[189] Liang W, Eliyahu D, Ilchenko VS, et al. High spectral purity Kerr frequency comb radio frequency photonic oscillator. Nat Commun 2015;6:7957.
[190] Xue X, Xuan Y, Kim H-J, et al. Programmable single-bandpass photonic RF filter based on Kerr comb from a microring. J Lightwave Technol 2014;32:3557–65.
[191] Alibart O, D'Auria V, Micheli MD, et al. Quantum photonics at telecom wavelengths based on lithium niobate waveguides. J Opt 2016;18:104001-1-32.
[192] Sharapova PR, Luo KH, Herrmann H, Reichelt M, Meier T, Silberhorn C. Toolbox for the design of $LiNbO_3$-based passive and active integrated quantum circuits. New J Phys 2017;19:123009.
[193] Fuerst JU, Strekalov D, Elser D, et al. Quantum light from a whispering-gallery-mode disk resonator. Phys Rev Lett 2011;106:113901.
[194] Tanzilli S, Tittel W, De Riedmatten H, et al. PPLN waveguide for quantum communication. Eur Phys J D 2002;18:155–60.
[195] Fujii G, Namekata N, Motoya M, Kurimura S, Inoue S. Bright narrowband source of photon pairs at optical telecommunication wavelengths using a type-II periodically poled lithium niobate waveguide. Opt Express 2007;15:12769–76.
[196] Jin H, Liu FM, Xu P, et al. On-chip generation and manipulation of entangled photons based on reconfigurable lithium–niobate waveguide circuits. Phys Rev Lett 2014;113:103601.
[197] Garg A, Mermin ND. Detector inefficiencies in the Einstein–Podolsky–Rosen experiment. Phys Rev D 1987;35:3831–5.
[198] Ladd TD, Jelezko F, Laflamme R, Nakamura Y, Monroe C, O'Brien JL. Quantum computers. Nature 2010;464:45–53.
[199] Gisin N, Thew R. Quantum communication. Nat Photonics 2007;1:165–71.
[200] Höpker JP, Gerrits T, Lita A, et al. Integrated transition edge sensors on titanium in-diffused lithium niobate waveguides. APL Photonics 2019;4:056103.
[201] Cabrera B, Clarke RM, Colling P, Miller AJ, Nam SW, Romani RW. Detection of single infrared, optical, and ultraviolet photons using superconducting transition edge sensors. Appl Phys Lett 1998;73:735–7.
[202] Sinclair N, Saglamyurek E, George M, et al. Spectroscopic investigations of a Ti:Tm:$LiNbO_3$ waveguide for photon-echo quantum memory. J Lumin 2010;130:1586–93.
[203] Udem T, Holzwarth R, Hansch TW. Optical frequency metrology. Nature 2002;416:233–7.
[204] Picqué N, Hänsch TW. Frequency comb spectroscopy. Nat Photonics 2019;13:146–57.
[205] Kayes MI and Rochette M. Precise distance measurement by a single electro-optic frequency comb. IEEE Photonic Tech L 2019;31:775–8.
[206] Yang L, Nie J, Duan L. Dynamic optical sampling by cavity tuning and its application in LiDAR. Opt Express 2013;21:3850–60.
[207] Hochrein T, Wilk R, Mei M, Holzwarth R, Krumbholz N, Koch M. Optical sampling by laser cavity tuning. Opt Express 2010;18:1613–7.
[208] Kayes MI and Rochette M. Optical frequency comb generation with ultra-narrow spectral lines. Opt Lett 2017;42:2718–21.
[209] Lee S-J, Widiyatmoko B, Kourogi M, Ohtsu M. Ultrahigh scanning speed optical coherence tomography using optical frequency comb generators. Jpn J Appl Phys 2001;40:L878.
[210] Shams-Ansari A, Yu M, Chen Z, et al. Microring electro-optic frequency comb sources for dual-comb spectroscopy. In: CLEO: Applications and Technology. Washington, DC, USA, Optical Society of America; 2019:JTh5B–8.
[211] He Y, Yang Q-F, Ling J, et al. Self-starting bi-chromatic $LiNbO_3$ soliton microcomb. Optica 2019;6:1138–44.
[212] Fallahpour A, Alishahi F, Zou K, et al. Demonstration of tunable optical aggregation of QPSK to 16-QAM over optically generated Nyquist pulse trains using nonlinear wave mixing and a Kerr frequency comb. J Lightwave Technol 2020;38:359–65.
[213] Yue W, Ding Y, Wu B, Shen Y. High-power mid-infrared picosecond pulse bunch generation through difference frequency generation. OSA Opt Lett 2020;45:383–86
[214] Miller DAB. Self-aligning universal beam coupler. Opt Express 2013;21:6360–70.
[215] Shen Y, Harris NC, Skirlo S, et al. Deep learning with coherent nanophotonic circuits. Nat Photonics 2017;11:441–6.
[216] Perez D, Gasulla I, Crudgington L, et al. Multipurpose silicon photonics signal processor core. Nat Commun 2017;8:636.
[217] Molesky S, Lin Z, Piggott AY, Jin W, Vuckovic J, Rodriguez AW. Inverse design in nanophotonics. Nat Photonics 2018;12:659–70.
[218] Thomas J, Heinrich M, Zeil P, et al. Laser direct writing: enabling monolithic and hybrid integrated solutions on the lithium niobate platform. Phys Status Solidi A 2011;208:276–83.

[219] Ooka Y, Tetsumoto T, Fushimi A, Yoshiki W, Tanabe T. CMOS compatible high-Q photonic crystal nanocavity fabricated with photolithography on silicon photonic platform. Sci Rep 2015;5:11312.
[220] Eichinger-Heue R, Glinsner T, Kettner P, et al. Nanoimprinting – a key enabling technology for BioMEMS and biomedical applications. In: Knobloch H, Kaminorz Y, editors. MicroNano integration. Berlin, Germany, Springer Berlin Heidelberg, 2004:137–46.
[221] Su Z, Hosseini ES, Timurdogan E, et al. Whispering gallery germanium-on-silicon photodetector. Opt Lett 2017;42:2878–81.
[222] Li N, Vermeulen D, Su Z. Monolithically integrated erbium-doped tunable laser on a CMOS-compatible silicon photonics platform. Opt Express 2018;26:16200–11.
[223] Brinkmann R, Baumann I, Dinand M, Sohler W, Suche H. Erbium-doped single- and double-pass Ti:$LiNbO_3$ waveguide amplifiers. IEEE J Quantum Elect 1994;30:2356–60.